ADVANCES IN ATMOSPHERIC SCIENCES, VOL. 42, APRIL 2025, 653–669

• **Original Paper** •

Effectiveness of Precursor Emission Reductions for the Control of Summertime Ozone and $PM_{2.5}$ in the Beijing–Tianjin–Hebei Region under Different Meteorological Conditions[※]

Jing QIAN and Hong LIAO[*]

Jiangsu Key Laboratory of Atmospheric Environment Monitoring and Pollution Control, Jiangsu Collaborative Innovation Center of Atmospheric Environment and Equipment Technology, School of Environmental Science and Engineering, Nanjing University of Information Science & Technology, Nanjing 210044, *Jiangsu, China*

(Received 22 February 2024; revised 12 April 2024; accepted 23 April 2024)

ABSTRACT

We used observed concentrations of air pollutants, reanalyzed meteorological parameters, and results from the Goddard Earth Observing System Chemical Transport Model to examine the relationships between concentrations of maximum daily 8-h average ozone (MDA8 O_3), $PM_{2.5}$ (particulate matter with diameter of 2.5 μm or less), and $PM_{2.5}$ components and 2-m temperature (T2) or relative humidity (RH), as well as the effectiveness of precursor emission reductions on the control of O_3 and $PM_{2.5}$ in Beijing–Tianjin–Hebei (BTH) under different summertime temperature and humidity conditions. Both observed (simulated) MDA8 O_3 and $PM_{2.5}$ concentrations increased as T2 went up, with linear trends of 4.8 (3.2) ppb $°C^{-1}$ and 1.9 (1.5) μg m^{-3} $°C^{-1}$, respectively. Model results showed that the decreases in MDA8 O_3 from precursor emission reductions were more sensitive to T2 than to RH. Reducing a larger proportion of volatile organic compound (VOC) emissions at higher T2 was more effective for the control of summertime O_3 in BTH. For the control of summertime $PM_{2.5}$ in BTH, reducing nitrogen oxides (NO_x) combined with a small proportion of VOCs was the best measure. The magnitude of reduction in $PM_{2.5}$ from reducing precursor emissions was more sensitive to RH than to T2, with the best efficiency at high RH. Results from this study are helpful for formulating effective policies to tackle O_3 and $PM_{2.5}$ pollution in BTH.

Key words: ozone, $PM_{2.5}$, emission reductions, meteorological conditions

Citation: Qian, J., and H. Liao, 2025: Effectiveness of precursor emission reductions for the control of summertime ozone and $PM_{2.5}$ in the Beijing–Tianjin–Hebei region under different meteorological conditions. *Adv. Atmos. Sci.*, **42**(4), 653–669, https://doi.org/10.1007/s00376-024-4071-4.

Article Highlights:

- Observed summertime concentrations of O_3 and $PM_{2.5}$ in BTH increased as T2 and RH increased (at RH < 60%).
- Larger percentage reductions of VOC emissions at higher temperature is more effective for alleviating summertime O_3 pollution in BTH.
- Reducing NO_x along with a small proportion of VOCs is the best measure for $PM_{2.5}$, which has the best effect at high RH.
- For the co-pollution of O_3 and $PM_{2.5}$ in summer in BTH, emission reductions have the best effect in a hot and humid conditions.

1. Introduction

China has high concentrations of both $PM_{2.5}$ (particulate matter with an aerodynamic equivalent diameter of 2.5 μm or less) and tropospheric ozone (O_3), especially in the Beijing–Tianjin–Hebei (BTH) region, a major urban cluster with developed economies in eastern China (Luo et al., 2022; Dai et al., 2023). Over 2013–19, the summer (June–July–August, JJA) mean maximum daily 8-h average (MDA8) O_3 concentrations were observed to increase at a rate of 3.3 ppb yr^{-1} over the North China Plain (NCP) (Li et al., 2020). In spite of the effective control of $PM_{2.5}$ pollution in China since the implementation of the Clean Air Action in 2013, the annual mean $PM_{2.5}$ concentration averaged over BTH was 44 μg m^{-3} in 2022 (https://english.mee.gov.cn/Resources/Reports/soe/, last accessed: 20 February, 2024), which still far exceeded the air quality standard of 5 μg m^{-3} set by the World Health Organization. Further efforts are needed to control O_3 and $PM_{2.5}$ pollution in BTH (Zhao

---

※ This paper is a contribution to the special topic on Air Pollution Complex Research in China: Recent Advances.

* Corresponding author: Hong LIAO
Email: hongliao@nuist.edu.cn

et al., 2021).

Variations of O_3 and $PM_{2.5}$ are highly sensitive to changes in meteorology. While wind, precipitation, and planetary boundary layer height may influence the dispersion, wet removal, and vertical mixing of air pollutants (Chen et al., 2020; Zhang and Wang, 2020), temperature and relative humidity (RH) play important roles in the formation of secondary pollutants and the gas-particle partitioning of semivolatile components (Wang et al., 2013; Shah et al., 2018; Leung et al., 2020). Higher temperature can accelerate the chemical production of O_3, while higher RH increases the O_3 loss (Johnson et al., 1999; Jacob and Winner, 2009). As for $PM_{2.5}$, higher temperature can enhance gas-phase reaction rates and oxidant concentrations, leading to higher sulfate (SO_4^{2-}) concentrations (Liao et al., 2006). However, higher temperature can promote the volatilization of ammonium nitrate (Kleeman, 2008). Higher RH is conducive to aqueous-phase aerosol chemistry for the formation of secondary $PM_{2.5}$ (Dawson et al., 2007; Zheng et al., 2015). Li et al. (2019a) showed by a stepwise multiple linear regression model that the changes in daily maximum 2-m temperature (Tmax), 10-m meridional wind, and RH explained 66% of monthly variability in summer MDA8 O_3 in BTH over 2013–17. By applying the Goddard Earth Observing System Chemical Transport Model (GEOS-Chem) and the Lindeman, Merenda, and Gold method, Dang et al. (2021) found that the changes in Tmax and RH explained, respectively, 31% and 11% of the simulated interannual variations of MDA8 O_3 in JJA of 2012–17 over the NCP in the simulation with changes in meteorological parameters alone. Zong et al. (2021) analyzed the synoptic weather patterns corresponding to the cooccurrence of O_3 and $PM_{2.5}$ pollution during summer of 2015–18 over eastern China by applying T-mode principal component analysis, and found that the warm and moist flow brought by the western Pacific subtropical high promoted hygroscopic growth of fine particulate matter, resulting in increases in $PM_{2.5}$ concentrations in BTH.

Emissions reduction is the primary measure for controlling air pollution. Owing to the absence of effective emission control measures on volatile organic compounds (VOCs) in previous policies in China, anthropogenic VOC emissions in China were estimated to increase from 25.9 Tg in 2010 to 28.6 Tg in 2017 (increase by 11%) according to the Multi-resolution Emission Inventory for China (Zheng et al., 2018). In the 14th Five-Year Plan for 2021–2025, China identifies VOC emissions management as a priority in order to further improve air pollution. In addition, as a common and important precursor of O_3 and $PM_{2.5}$, the continuous control of nitrogen oxides ($NO_x = NO + NO_2$) emissions remains a key focus of air pollution control. A number of studies have examined VOCs and NO_x emission reduction strategies for the synergistic reduction of ambient O_3 and $PM_{2.5}$ pollution. By using simulations from GEOS-Chem for summer of 2017, Li et al (2019b) evaluated the effects of the reduction targets for 2018–2020 (i.e., 9% for NO_x emissions, 10% for VOC emissions and 8% for $PM_{2.5}$ concentrations) over the NCP, and showed that the increases in O_3 owing to the decreases in $PM_{2.5}$ were offset by the decreases in O_3 owing to the decreases in NO_x and VOC emissions, resulting in the reduction of about 1 ppb in the seasonal mean MDA8 O_3. Xiang et al. (2020), by applying the Weather Research and Forecasting (WRF) model with Chemistry together with an empirical kinetics modeling approach, conducted multiple scenario analyses for reduction of anthropogenic NO_x and VOC emissions over BTH and surrounding areas relative to January and July of 2015–17, and suggested, from a long-term perspective, reducing firstly VOC emissions by about 60% and NO_x emissions by about 20% to avoid the rebound of O_3, and then phasing out the remaining emissions to reach a deep mitigation. Ding et al. (2022) adopted the Community Multiscale Air Quality model, WRF model, and an extended response surface model with polynomial functions, and reported that no matter how much VOC emissions was reduced, NO_x emissions reduction (64%–81%) was essential to attain the air quality standard (with an annual $PM_{2.5}$ concentration $\leqslant$ 35 μg m^{-3} and annual 90th percentile MDA8 O_3 concentration $\leqslant$ 160 μg m^{-3}) in BTH in 2017, in which year the observed annual concentrations of O_3 and $PM_{2.5}$ were 178–216 and 57–86 μg m^{-3}, respectively. These studies with the impacts of VOCs and NO_x emission reductions on O_3 and $PM_{2.5}$ were generally based on the average over certain time scales (i.e., monthly, seasonal, annual), ignoring the impacts of variations in meteorological fields on control measures. Therefore, it is essential to examine the effectiveness of precursor emission reductions for the control of O_3 and $PM_{2.5}$ pollution under different conditions of temperature and humidity so as to formulate more effective policies.

The objectives of this study are (1) to examine the relationships between concentrations of O_3 and $PM_{2.5}$ and 2-m temperature (T2) or RH based on observations from the Chinese Ministry of Ecology and Environment (MEE) and the reanalyzed meteorological parameters from Version 2 of the Modern-Era Retrospective Analysis for Research and Applications (MERRA-2) over BTH for the summer of 2019, (2) to apply the GEOS-Chem model that can capture the observed relationships to quantify the effectiveness of emission reductions of VOCs and NO_x on O_3 and $PM_{2.5}$ in BTH under different conditions of temperature and humidity, and (3) to identify the temperature and humidity conditions under which emission reductions have the best effect for alleviating summertime O_3 and $PM_{2.5}$ pollution in BTH. The year 2019 was selected because MDA8 O_3 concentrations in this year were among the highest in recent years, and the concentrations of $PM_{2.5}$ in 2019 were still at a relatively high level in BTH.

The remainder of this paper is structured as follows. Section 2 describes the observations, reanalyzed meteorological data, GEOS-Chem model, and numerical experiments. Evaluation of the model, the relationships between atmospheric oxidants, O_3, $PM_{2.5}$, and $PM_{2.5}$ components and T2 or RH, as well as the simulated changes of all these species under different temperature and humidity conditions with emission reductions of VOCs and/or NO_x are presented in section 3. Section 4 summarizes the main conclusions.

2. Methods

2.1. *Observed O_3 and $PM_{2.5}$ concentrations*

The observed hourly concentrations of O_3 and $PM_{2.5}$ for JJA 2019 were obtained from the MEE and can be downloaded from https://quotsoft.net/air/ (in Chinese, last accessed: 20 February 2024). There are over 1600 observational sites throughout the country, of which 79 are located in the BTH region (37°–41°N, 114°–118°E). Concentrations are reported by the MEE in units of $\mu g\ m^{-3}$ under the reference state (298 K, 1013 hPa) for O_3 and under the local ambient state for $PM_{2.5}$. For consistency between observed and simulated O_3 concentrations, we converted the units of observed O_3 into ppb. For O_3, MDA8 was used in this study, which was calculated when there were valid hourly data for at least 6 h for each 8 h and there were more than 14 valid 8-h averaged data in each day. The daily mean $PM_{2.5}$ concentration was calculated when there were valid hourly data for more than 20 h during that day. All the site concentrations were averaged within each of the 0.5° latitude × 0.625° longitude grid cells of MERRA-2 for model evaluation and subsequent analysis, following Dai et al. (2023). There are 18 model grid cells in BTH. We consider each day of each grid cell as an independent sample.

2.2. *Reanalyzed meteorological data*

Meteorological fields for 2019 were obtained from MERRA-2, generated by NASA's Global Modeling and Assimilation Office. The MERRA-2 data have a horizontal resolution of 0.5° latitude × 0.625° longitude. Meteorological parameters considered in this study include T2, RH, and precipitation (PR). The temporal resolution for T2 and PR is 1 h, and that for RH is 3 h. Note that T2 and RH are averaged over 24 h, while PR is summed over 24 h. We do not consider days with PR; samples with total daily PR greater than 0.1 mm were removed. Meanwhile, after removing the days with missing data of MDA8 O_3 or $PM_{2.5}$, there are ultimately 620 valid samples remaining out of 1656 samples over BTH in JJA 2019. To explore the effects of precursor emission reductions on MDA8 O_3 and $PM_{2.5}$ under different conditions of temperature and humidity, the T2 data are binned to 2°C intervals and the RH data to 5% intervals.

2.3. *GEOS-Chem model*

The simulations of air pollutants for JJA 2019 were carried out using the nested version of GEOS-Chem (version 11-01, http://wiki.seas.harvard.edu/geos-chem/index.php/GEOS-Chem_v11-01, last accessed: 20 February 2024), driven by the MERRA-2 assimilated meteorological fields (Gelaro et al., 2017). The nested version of v11-01 in the Asian domain (11°S–55°N, 60°–150°E) has a horizontal resolution of 0.5° latitude × 0.625° longitude and 47 vertical layers up to 0.01 hPa, with dynamical boundary conditions from a global GEOS-Chem simulation of 2° latitude × 2.5° longitude horizontal resolution. The O_3 and $PM_{2.5}$ simulation in the GEOS-Chem model has been extensively used in previous studies (Fu and Liao, 2014; Zhang et al., 2018; Wang and Liao, 2020; Gong et al., 2022). The GEOS-Chem model includes fully coupled O_3–NO_x–hydrocarbon chemistry (Bey et al., 2001; Park et al., 2004) and aerosols including SO_4^{2-} (Park et al., 2004), nitrate (NO_3^-) (Pye et al., 2009), ammonium (NH_4^+), black carbon (BC), and organic carbon (OC) (Park et al., 2003), mineral dust (Fairlie et al., 2007), and sea salt (Alexander et al., 2005). Two primary organic aerosol (POA) tracers are considered in the model: hydrophobic and hydrophilic POAs. The hydrophobic POA becomes hydrophilic with an *e*-folding time of 1.15 days (Cooke et al., 1999; Park et al., 2003). It is assumed that 50% of POAs emitted are hydrophobic (Park et al., 2003). The simulation of secondary organic aerosol (SOA) is based on the volatility basis set approach. Reactions of forming SOA from different parent hydrocarbons can be mapped onto the same set of bins encompassing the range of typical ambient organic aerosol mass concentrations (~0.1–100 $\mu g\ m^{-3}$) (Jo et al., 2013). Wet deposition, including washout, rainout, and scavenging in moist convective updrafts, follows the scheme of Liu et al. (2001). Dry deposition is calculated based on the resistance-in-series model described by Wesely (1989) with a number of modifications (Wang et al., 1998).

The anthropogenic emissions of NO_x, carbon monoxide, OC, BC, sulfur dioxide (SO_2), and ammonia (NH_3) were obtained from MEIC (Multi-resolution Emission Inventory Model for Climate and air pollution research; http://meicmodel.org.cn/?page_id=2351&lang=en, last accessed: 20 February 2024) for the year 2019, which includes emissions from the industry, power, residential, and transportation sectors. Due to the selection of a chemical mechanism developed by the State Air Pollution Research Center (SAPRC), namely SAPRC99, the downloaded MEIC data lack aromatic species that have a significant impact on SOA formation, such as benzene and toluene (Zhang et al., 2021; Wang et al., 2022). As a result, the anthropogenic emissions of VOCs (including ethane, propane, butanes, pentanes, other alkanals, ethene, propene, acetylene, benzene, toluene, xylene, formaldehyde, total ketones, and total acids) were obtained from the Shared Socioeconomic Pathway (SSP) emissions inventory (https://esgf-node.llnl.gov/projects/input4mips/, last accessed: 20 February 2024). Year-2020 emissions of SSP2-4.5 were used in our simulations, which represent a middle-of-the-road development in the mitigation and adaptation challenges space. The biogenic emissions in GEOS-Chem were taken from MEGAN v2.1 (Guenther et al., 2012).

2.4. *Numerical experiments*

To investigate the effects of VOC emission reductions on O_3 and $PM_{2.5}$ in BTH under different meteorological conditions, four numerical experiments were performed for JJA 2019. Considering the recent national policies and the feasibility of practical control measures, the reduction ratios of anthropogenic VOCs were set between 10% and 50% with a 20% interval:

(1) CTRL: Control simulation without emission control measures;

(2) VOCs_10: The same as CTRL but with a 10% reduction in anthropogenic VOC emissions in China;

(3) VOCs_30: The same as CTRL but with a 30% reduction in anthropogenic VOC emissions in China;

(4) VOCs_50: The same as CTRL but with a 50% reduction in anthropogenic VOC emissions in China;

Since NO_x also plays an important role in the formation of O_3 and $PM_{2.5}$, and considering the new 14th Five-Year Plan for 2021–25 calls for a 10% decrease in NO_x emissions, we also conducted three additional experiments:

(1) NO_x_10+VOCs_10: The same as CTRL but with a 10% reduction in both anthropogenic NO_x and anthropogenic VOC emissions in China;

(2) NO_x_10+VOCs_30: The same as CTRL but with 10% and 30% reductions in anthropogenic NO_x and VOC emissions in China, respectively;

(3) NO_x_10+VOCs_50: The same as CTRL but with 10% and 50% reductions in anthropogenic NO_x and VOC emissions in China, respectively;

All the simulations were integrated for the period of 1 June to 31 August 2019 after a six-month spin-up of the model.

3. Results

3.1. *Evaluation of model performance*

Figures 1a and b present, respectively, the spatial distribu-

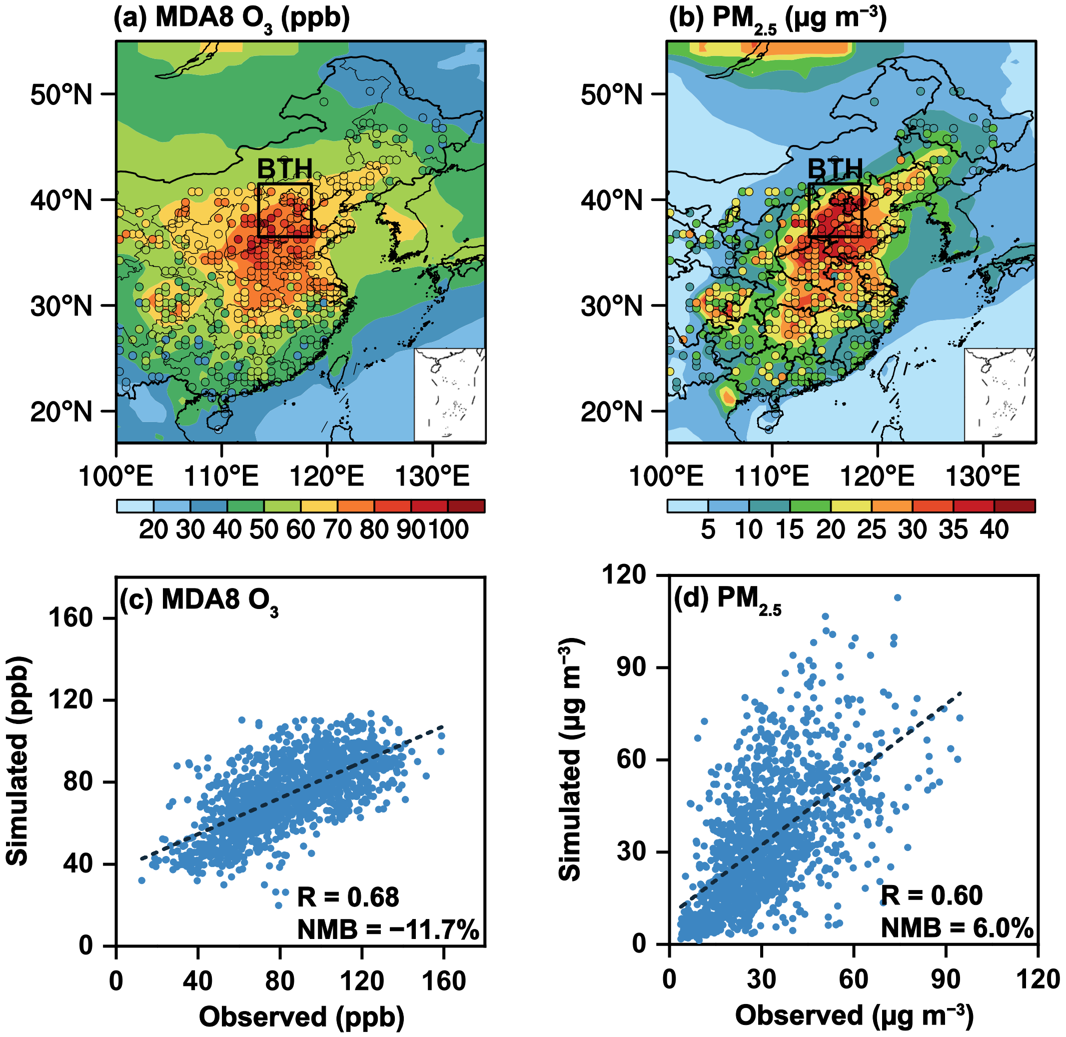

Fig. 1. (a, b) Spatial distributions of simulated (color shading) and observed (dots) surface-layer concentrations of (a) MDA8 O_3 (units: ppb) and (b) $PM_{2.5}$ (units: μg m^{-3}) averaged over summer 2019. The solid black rectangles in (a, b) indicate the BTH region, which contain 18 grid cells. (c, d) Scatterplots of simulated versus observed daily concentrations of (c) MDA8 O_3 (units: ppb) and (d) $PM_{2.5}$ (units: μg m^{-3}) for the 18 grid cells located in BTH. The correlation coefficient (*R*) and normalized mean bias (NMB; %) are also shown. Here, *R* is the correlation coefficient between simulated and observed concentrations. NMB = $\left[\sum_{i=1}^{N}(M_i - O_i)\right] / \sum_{i=1}^{N} O_i \times 100\%$, where O_i and M_i are the observed and simulated concentrations, respectively; *i* refers to the *i*th sample, and *N* is the total number of samples.

tions of simulated and observed surface-layer concentrations of MDA8 O_3 and $PM_{2.5}$ averaged over summer 2019. For model evaluation, observed MDA8 O_3 and $PM_{2.5}$ concentrations were averaged over all sites within each of the 0.5° × 0.625° MERRA-2 grid cells. The concentrations of MDA8 O_3 and $PM_{2.5}$ were both relatively high in BTH. The seasonal mean observed (simulated) concentrations of MDA8 O_3 and $PM_{2.5}$ were 83.6 (71.9) ppb and 31.6 (32.1) μg m^{-3}, respectively, as values were averaged over the 18 grids in BTH. Figures 1c and d show scatterplots of simulated versus observed daily MDA8 O_3 and $PM_{2.5}$ concentrations, respectively, for the 18 grid cells located in BTH. The simulated spatiotemporal variations of MDA8 O_3 and $PM_{2.5}$ agree fairly well with the observations, with correlation coefficients (R) of 0.68 and 0.60, respectively. The model underestimates MDA8 O_3 concentrations with a normalized mean bias (NMB) of −11.7% and overestimates $PM_{2.5}$ concentrations with an NMB of +6.0% in BTH.

3.2. *Relationships between atmospheric oxidants and T2 or RH*

The concentrations of total oxidants ($O_x = O_3 + NO_2$), hydroxyl radical (OH), and nitrogen trioxide (NO_3) are usually used to characterize the atmospheric oxidation capacity (Kang et al., 2021; Tang et al., 2022). Figures 2a–c and 2d–f show boxplots of the simulated daily concentrations of O_x, OH, and NO_3 in T2 bins and in RH bins (described in section 2.2), respectively, considering the 18 grid cells of BTH in JJA 2019 (620 valid samples as also described in section 2.2) from the CTRL simulation to investigate the levels of atmospheric oxidation capacity under different temperature and humidity conditions. The O_x and NO_3 concentrations gradually increased as T2 went up, with the mean values increasing from 44.2 and 5.0×10^{-3} ppb in the bin of ≤ 20°C to 81.3 and 3.3×10^{-2} ppb in the bin of > 32°C, respectively. The concentrations of OH exhibited continuous increases as T2 was above 24°C, and the mean value increased from 2.5×10^6 molecule cm^{-3} at a T2 of 24°C–26°C to 3.3×10^6 molecule cm^{-3} at > 32°C. The relationships between concentrations of O_x, OH, or NO_3 and T2 indicate that the atmospheric oxidation capacity is stronger at higher temperature, which favors the formation of both secondary inorganic and organic particulates (Feng et al., 2019). As for the relationships between atmospheric oxidation capacity and RH, there was a small increasing trend in simulated O_x concentrations as RH increased, with a peak value of 69.5 ppb when RH was 45%–50%. OH concentrations showed a W-shaped trend, with valleys occurring when RH values were 35%–40% and 50%–55%. NO_3 concentrations had an overall decreasing trend as RH increased.

3.3. *Relationships between air pollutants and T2 or RH*

3.3.1. *Relationships between concentrations of MDA8 O_3 and $PM_{2.5}$ and T2 or RH*

Figure 3 displays the relationships between observed

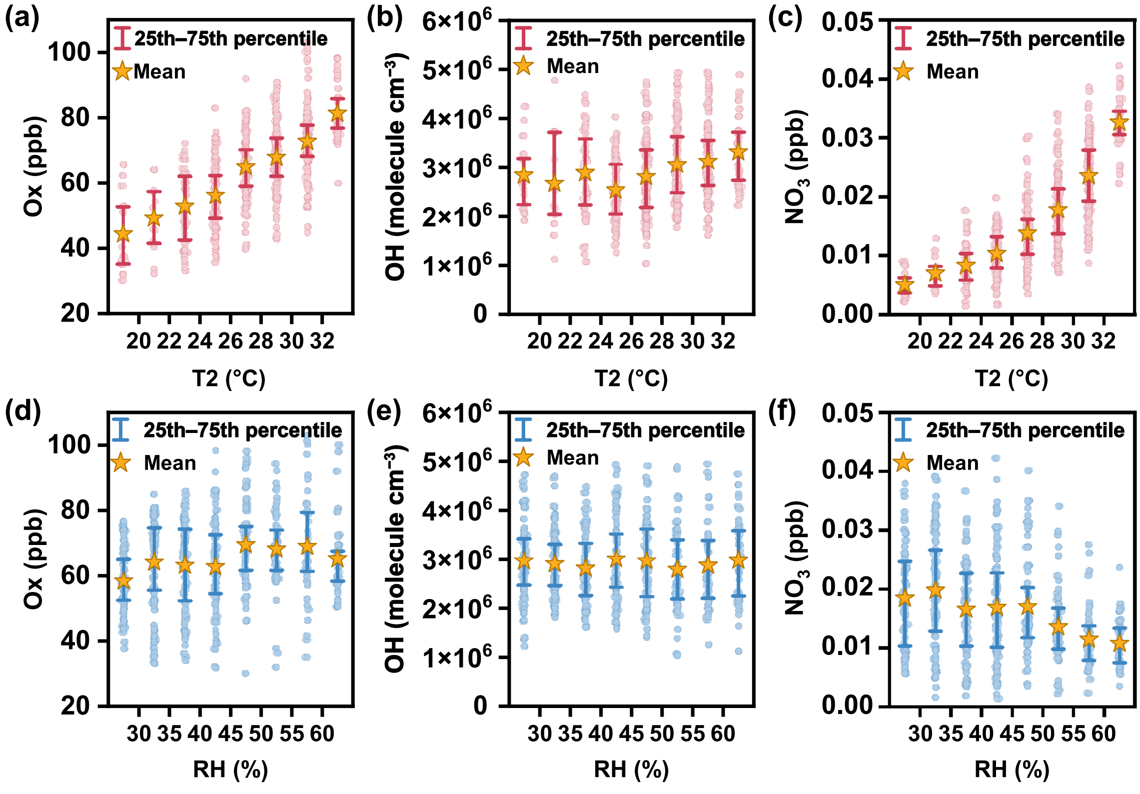

Fig. 2. Boxplots of surface-layer (a, d) total oxidants (O_x; units: ppb), (b, e) hydroxyl radicals (OH; units: molecule cm^{-3}), and (c, f) nitrogen trioxide (NO_3; units: ppb) in each T2 and RH bin in the 18 grid cells of BTH in JJA 2019 (620 valid samples) from the CTRL simulation. The T2 results are binned to 2°C intervals and RH to 5% intervals.

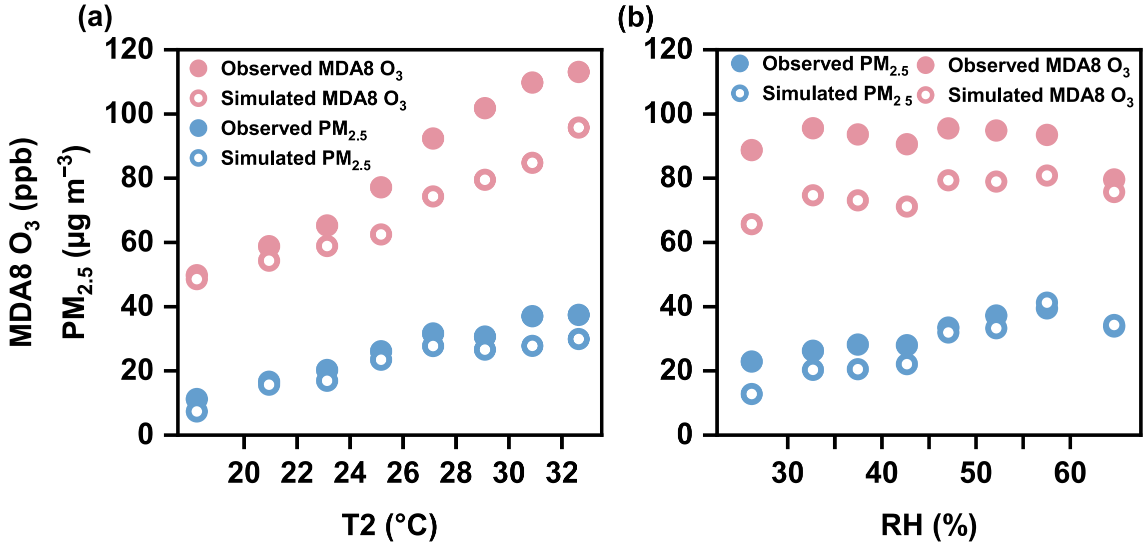

Fig. 3. Relationships between observed (solid dots) and simulated (open dots) concentrations of MDA8 O_3 (pink dots) and $PM_{2.5}$ (blue dots) and (a) T2 or (b) RH in the 18 grid cells of BTH in JJA 2019 (620 valid samples). Dots represent the mean of the daily concentrations of MDA8 O_3 (units: ppb) and $PM_{2.5}$ (units: $\mu g\ m^{-3}$) (a) versus daily T2 (units: °C) in each T2 bin or (b) versus daily RH (%) in each RH bin. T2 results are binned to 2°C intervals and RH to 5% intervals.

and simulated concentrations of MDA8 O_3 and T2 or RH in BTH during JJA 2019 (620 valid samples as described in section 2.2). Both observed and simulated MDA8 O_3 increased as T2 went up, with increasing rates of 4.8 and 3.2 ppb $°C^{-1}$, respectively. As RH increased, there was a bimodal feature in observed and simulated MDA8 O_3 concentrations, with the peaks appearing when RH values were 30%–35% and 45%–50% for observations (30%–35% and 55%–60% for model results). Both observed and simulated MDA8 O_3 concentrations decreased when RH was greater than 60%. Compared to 55%–60%, the net chemical production of O_3 had smaller positive values in the lower troposphere at RH > 60% (Fig. 6c). In addition, the concentration of BC (a chemically inert species) also showed a drop when RH was above 60% (Fig. 4j), indicating that physical processes also contributed to the decrease in pollutant concentrations.

The relationships between observed and simulated concentrations of $PM_{2.5}$ and T2 or RH in BTH during JJA 2019 are also shown in Fig. 3. On the whole, concentrations of observed (simulated) $PM_{2.5}$ also increased as T2 rose, with linear trends of 1.9 (1.5) $\mu g\ m^{-3}\ °C^{-1}$. $PM_{2.5}$ concentrations exhibited fast increases when T2 was between ⩽ 20°C and 26°C–28°C, but had a small drop when T2 was 28°C–30°C, and remained relatively stable when T2 was > 30°C. As RH increased from ⩽ 30% to 55%–60%, observed and simulated $PM_{2.5}$ concentrations continuously increased. The same as for MDA8 O_3, $PM_{2.5}$ concentrations decreased significantly when RH was above 60%. At 1005–913 hPa, net chemical production of $PM_{2.5}$ had larger values at RH > 60% than those in the previous humidity interval (Fig. 6d), so physical processes dominated the drop in $PM_{2.5}$ at RH > 60%, as again indicated by the drop in BC concentration. The model generally captures the variations in the observed concentrations of MDA8 O_3 and $PM_{2.5}$ with T2 or RH.

3.3.2. *Relationships between $PM_{2.5}$ components and T2 or RH*

Figures 4a–e and 4f–i show the simulated surface concentrations of $PM_{2.5}$ components (BC, SO_4^{2-}, NO_3^-, NH_4^+, and SOA) and the vertical distributions of concentrations of SO_4^{2-}, NO_3^-, NH_4^+, and total nitrate($NO_3^T = HNO_3 + NO_3^-$), respectively, in T2 bins over BTH during JJA 2019 from the CTRL simulation. The concentrations are averaged over the 18 grid cells in BTH. As T2 increased, the mean concentrations of BC had a general upward trend. Since BC is assumed to be chemically inert in the model (Dang and Liao, 2019), changes in BC concentrations can represent the changes in pollutant concentrations by physical processes. The relationship between BC and T2 indicates that physical processes were generally more conducive to the accumulation of pollutants at higher temperature. To identify the contributions of chemical processes to concentrations under different temperatures, the vertical profiles of net chemical production of SO_4^{2-}, NO_3^-, and NH_4^+ in each T2 bin in the 18 grid cells of BTH during JJA 2019 are shown in Figs. 5a–c. In the lower troposphere (from the surface to the altitude of approximately 700 hPa), the chemical production of SO_4^{2-} gradually increased when T2 increased (Fig. 5a), consistent with the trends of atmospheric oxidants (Figs. 2a–c). Therefore, both physical and chemical processes contributed to the increases in SO_4^{2-} concentrations as T2 increased (Fig. 4b).

For the formation of total nitrate, NO_2 oxidation by OH by $NO_2+OH+M \rightarrow HNO_3+M$ is the major pathway during daytime, and the major reactions at nighttime are $NO+O_3 \rightarrow NO_2+O_2$, $NO_2+O_3 \rightarrow NO_3+O_2$, $NO_2+NO_3+M \rightarrow N_2O_5+M$, and $N_2O_5+H_2O \rightarrow 2HNO_3$ (Dong et al., 2014; Leung et al., 2020). Higher concentrations of NO_3^T at higher temperature (Fig. 4i) also confirms the enhancement of atmo-

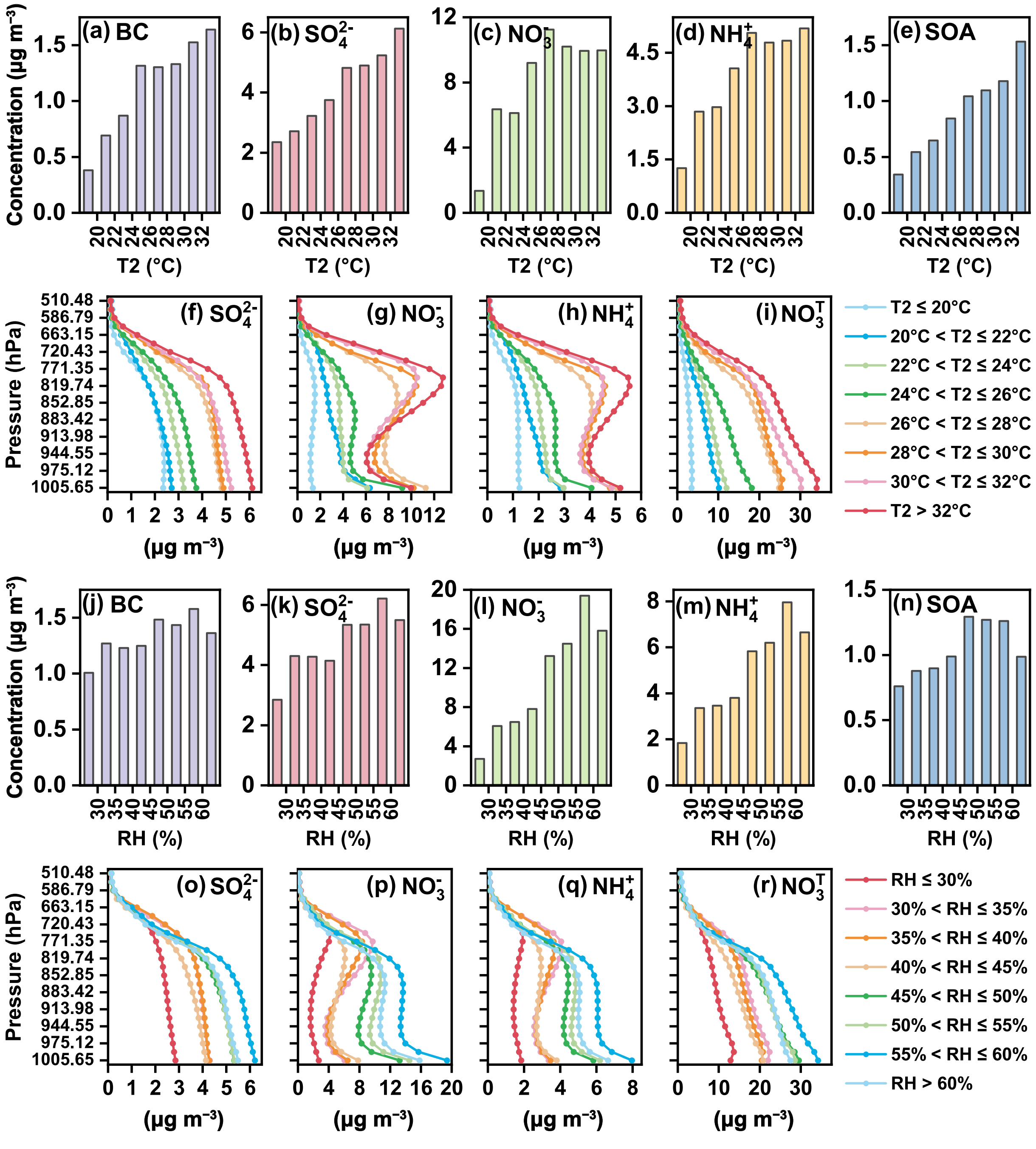

Fig. 4. The (a–e, j–n) surface concentrations (units: μg m^{-3}) of $PM_{2.5}$ components (BC, SO_4^{2-}, NO_3^-, NH_4^+, and SOA) and (f–i, o–r) vertical distributions of concentrations (units: μg m^{-3}) of SO_4^{2-}, NO_3^-, NH_4^+, and total nitrate (NO_3^T = HNO_3 + NO_3^-) averaged over each T2 or RH bin in the 18 grid cells of BTH in JJA 2019 (620 valid samples) from the CTRL simulation.

spheric oxidation capacity. However, the variation of NO_3^- concentrations with T2 differed from that of NO_3^T. The surface concentration of NO_3^- at a T2 of 22°C–24°C was lower than that at 20°C–22°C (Fig. 4c), due to the larger negative net chemical production from the surface to 913 hPa at 22°C–24°C (Fig. 5b). Similarly, relative to 26°C–28°C, the net chemical production of NO_3^- had larger negative values from the surface to 913 hPa, and consequently the surface NO_3^- had a lower concentration at a T2 of 28°C–30°C. At 959–898 hPa, the net chemical production of NO_3^- was more negative, both at 30°C–32°C and at > 32°C, than those in the previous temperature interval, resulting in the decreases in NO_3^- concentrations as T2 increased. Overall, in the lower troposphere, the lower concentrations of NO_3^- at higher T2 could be attributed to the evaporation of NO_3^-. For NH_4^+, as a result of the larger negative net chemical production from the surface to 913 hPa at 28°C–32°C (Fig. 5c), concentrations at 28°C–32°C were lower than those at

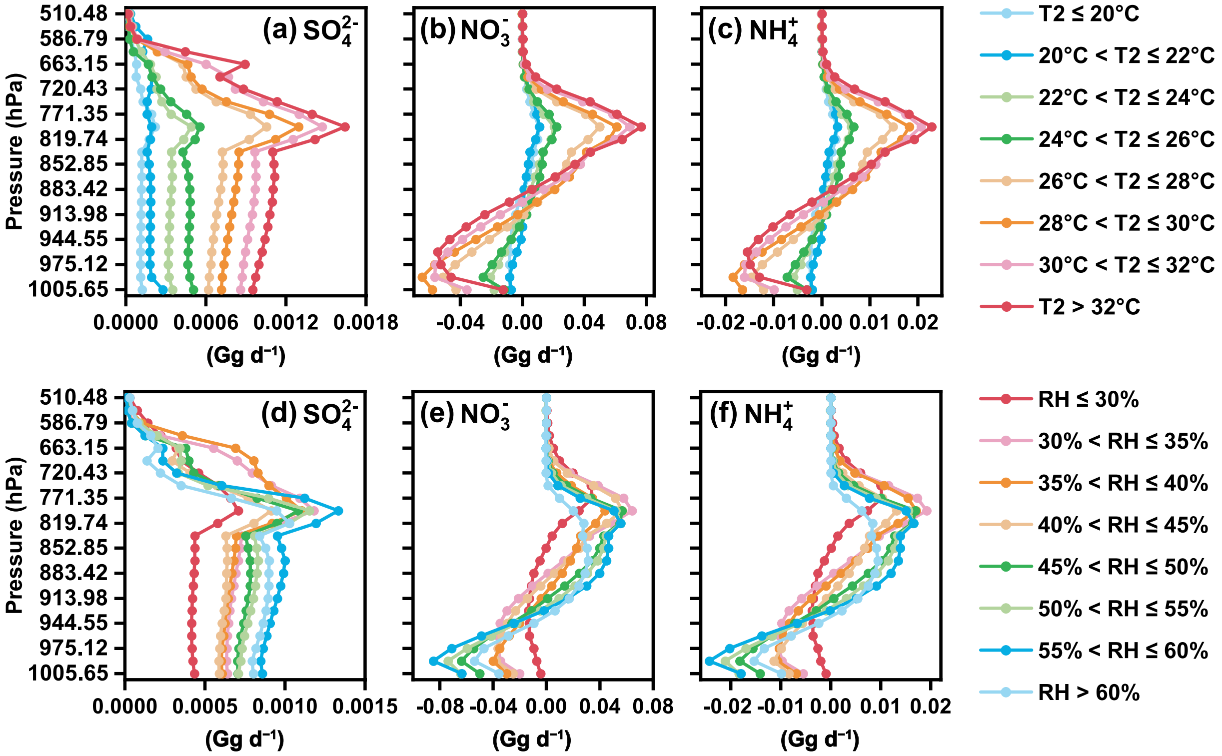

Fig. 5. Vertical profiles of net chemical production (units: Gg d^{-1}) of (a, d) SO_4^{2-}, (b, e) NO_3^-, and (c, f) NH_4^+ in each T2 or RH bin in the 18 grid cells of BTH in JJA 2019 (620 valid samples) from the CTRL simulation.

26°C–28°C (Fig. 4d).

High temperature promotes the evaporation of SOA and the emission of biogenic VOCs (Lee et al., 2011; Liu et al., 2019; Wu et al., 2020). The significant upward trend in SOA concentrations indicates the dominant roles of the elevated levels of biogenic VOC emissions and the enhanced atmospheric oxidation capacity as T2 went up. Simulated SOA concentrations were the lowest among all secondary aerosols, so it should not drive the trend of changes in $PM_{2.5}$ with T2.

The simulated surface and vertical concentrations of $PM_{2.5}$ components in RH bins in BTH during JJA 2019 are presented in Figs. 4j–r, and the change in net chemical production of secondary inorganic components with RH is presented in Figs. 5d–f. As RH increased, the mean concentrations of BC showed a fluctuating upward trend and a large drop when RH was above 60%, with three peaks appearing at 30%–35%, 45%–50%, and 55%–60% (Fig. 4j). SO_4^{2-} concentrations mimicked the variations in BC to some extent. Different from the changes in SO_4^{2-} concentrations, the concentrations of NO_3^- gradually increased with RH when RH was below 60%, and the changes in NH_4^+ followed those of NO_3^- (Figs. 4l and m). For SOA, the concentration increased first and then decreased as RH went up, with a peak concentration of 1.3 μg m^{-3} occurring when RH was 45%–50%. Consistent with BC, concentrations of $PM_{2.5}$ secondary components showed a significant drop at RH > 60%, indicating the role of physical processes. With respect to the role of chemical processes, the net chemical production of SO_4^{2-} generally increased with RH, whereas that of NO_3^- and NH_4^+ had larger net loss at higher RH (Figs. 5d–f).

3.4. *Impact of precursor emission reductions under different T2 and RH conditions*

3.4.1. *Impact of precursor emission reductions on atmospheric oxidants*

Six numerical experiments (VOCs_10, VOCs_30, VOCs_50, NO_x_10+VOCs_10, NO_x_10+VOCs_30, and NO_x_10+VOCs_50) were conducted to quantify the impacts of different proportions of precursor emissions reduction in summer 2019 on O_3 and $PM_{2.5}$ in the BTH region under different temperature and humidity conditions. Figures 7a–d and 7e–h show the mean changes (Δ) of OH, O_3, NO_3, and sulfur oxidation ratio (SOR = n-SO_4^{2-} / (n-SO_4^{2-} + n-SO_2), where n-SO_4^{2-} and n-SO_2 are the molar concentrations of SO_4^{2-} and SO_2, respectively) in T2 bins and in RH bins, respectively, relative to the CTRL simulation. SOR is used to quantify the conversion degrees of sulfur (Zhu et al., 2019).

The main sources of OH radicals in urban areas are produced by the photolysis of O_3, formaldehyde, and nitrous acid (HONO), and the main sink of OH is to react with NO_x, VOCs, and peroxy radicals (Li et al., 2021; Dai et al., 2024). Concentrations of OH mostly increased in the sensitivity simulations with emissions reductions relative to the CTRL simulation. Further investigation showed that in cases of reducing VOC emissions alone, the increase in OH concentration was mainly driven by the enhancement of photolysis of HONO, while in cases of simultaneously reducing

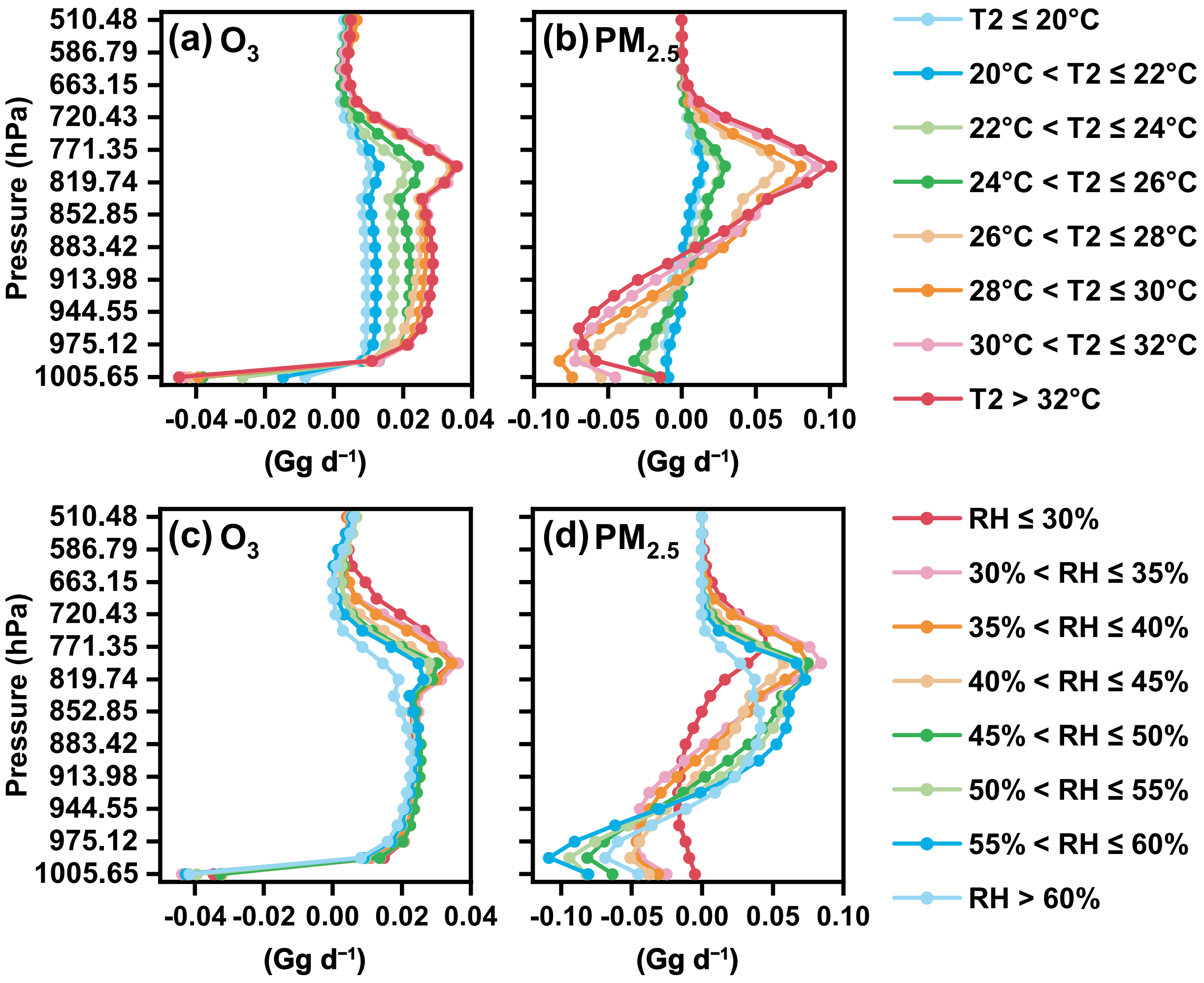

Fig. 6. As in Fig. 5 but for (a, c) O_3 and (b, d) $PM_{2.5}$.

NO_x and VOC emissions, it could mainly be attributed to weakening of the removal reaction with NO_2. As T2 increased, ΔOH concentrations peaked at 20°C–22°C in cases with reductions of VOC emissions alone, and peaked at 24°C–26°C in cases with reductions of both VOC and NO_x emissions, with the largest reduction of NO_x in this interval (Fig. 8a). ΔOH concentrations had a maximum value at RH of 45%–50% except for the cases of NO_x_10+VOCs_10 and NO_x_10+VOCs_30 simulations, which peaked at > 60%. ΔOH was larger when the percentage reduction of VOCs was higher. Compared to the cases with reductions of VOC emissions alone, simultaneous reductions of NO_x and VOCs promoted the formation of OH radicals when T2 was above 24°C and in almost each RH interval.

Concentrations of O_3 and NO_3 mostly decreased in the sensitivity simulations relative to the CTRL simulation. ΔO_3 and ΔNO_3 had larger negative values when T2 increased in all six simulations. When RH was lower than 60%, ΔO_3 had larger negative values as RH increased. The highest reductions in NO_3 concentrations occurred at RH of 30%–35% (45%–50%) in cases with reductions of VOC emissions alone (of both VOC and NO_x emissions). The larger the percentage reduction in VOC emissions, the higher the decreases in O_3 and NO_3. Reducing both NO_x and VOC emissions suppressed the decreases in O_3 and NO_3 concentrations relative to reducing VOC emissions alone.

ΔSOR was generally positive in the sensitivity simulations relative to the CTRL simulation. ΔSOR increased when T2 went up, except for the case of NO_x_10+VOCs_10, in which the highest increase occurred at 20°C–22°C. The maximum ΔSOR occurred when RH was 50%–55% (above 55%) in cases with reductions of VOC emissions alone (of both NO_x and VOC emissions). The simulation with a larger reduction in VOC emissions led to a greater increase in SOR.

3.4.2. *Impact of precursor emission reductions on MDA8 O_3 concentrations*

The absolute and percentage changes in MDA8 O_3 concentrations in each T2 and RH interval in BTH in JJA 2019 with the six emission reduction measures are summarized in Fig. 9. The changes in mean MDA8 O_3 concentrations were always negative. As T2 went up, the absolute values of ΔMDA8 O_3 gradually increased, with maximum values of 0.9, 2.7, 4.7, 3.4, and 5.2 ppb in the simulations of VOCs_10, VOCs_30, VOCs_50, NO_x_10+VOCs_30, and

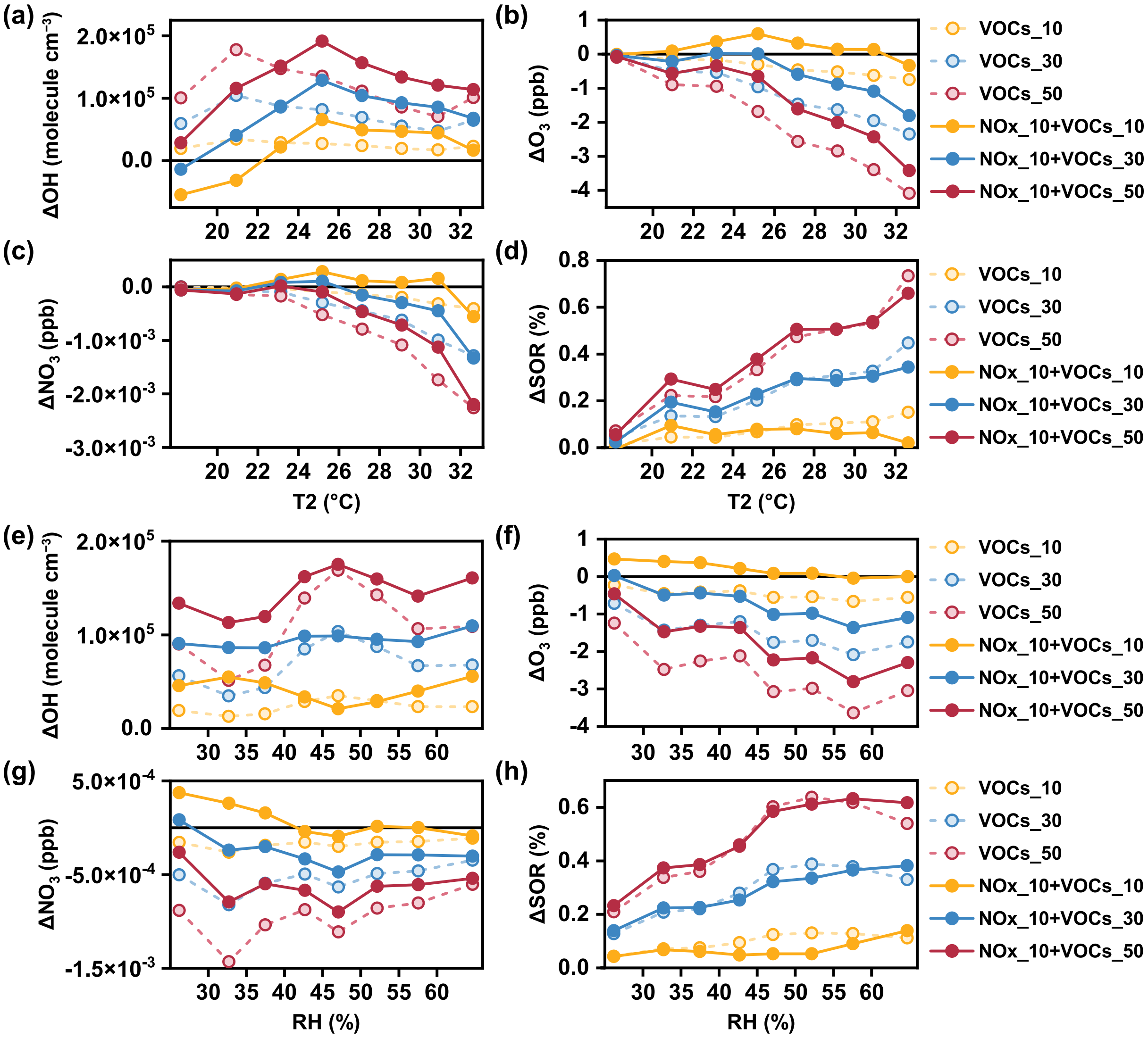

Fig. 7. Simulated mean changes in surface-layer (a, e) OH (units: molecule cm^{-3}), (b, f) O_3 (units: ppb), (c, g) NO_3 (units: ppb), and (d, h) sulfur oxidation ratio (SOR; units: %) in each T2 or RH bin in the 18 grid cells of BTH in JJA 2019 (620 valid samples) in simulations with reductions of anthropogenic VOC emissions alone (dotted lines with open dots) and simulations with simultaneous reductions of anthropogenic NO_x and VOC emissions (solid lines with solid dots) relative to the CTRL simulation.

NO_x_10+VOCs_50, respectively. In the NO_x_10+VOCs_10 simulation, although the decreases in MDA8 O_3 concentrations did not increase monotonically with T2, the decreases in the 75th percentile of MDA8 O_3 did (Fig. 10). As for the percentage changes in MDA8 O_3, the NO_x_10+VOCs_10, NO_x_10+VOCs_30, and NO_x_10+VOCs_50 simulations had the lowest values (−1.7%, −3.5%, and −5.4%, respectively) at T2 > 32°C, while the VOCs_10, VOCs_30, and VOCs_50 simulations exhibited the lowest values (−0.9%, −2.8%, and −4.9%, respectively) at 30°C–32°C. When RH increased, the absolute and percentage decreases of MDA8 O_3 concentrations both exhibited a bimodal trend, with the peaks appearing at RH of 30%–35% and 45%–50% in the NO_x_10+VOCs_10 simulation and at 30%–35% and 55%–60% in other simulations. The highest reductions were simulated to be 0.8 (1.0%), 2.6 (3.1%), 4.6 (5.4%), 1.0 (1.2%), 2.7 (3.1%), and 4.5 ppb (5.2%) in the VOCs_10, VOCs_30, VOCs_50, NO_x_10+VOCs_10, NO_x_10+VOCs_30, and NO_x_10+VOCs_50 simulations, respectively.

In summary, implementing precursor emission reductions can effectively mitigate summer O_3 pollution in BTH, especially in cases with higher reductions of VOC emissions. Furthermore, relative to the situation in RH intervals, a larger reduction of VOC emissions at higher T2 (> 30°C) showed better effectiveness in controlling O_3 pollution.

3.4.3. *Impact of precursor emission reductions on $PM_{2.5}$ concentrations*

Figure 11 shows the absolute and percentage changes

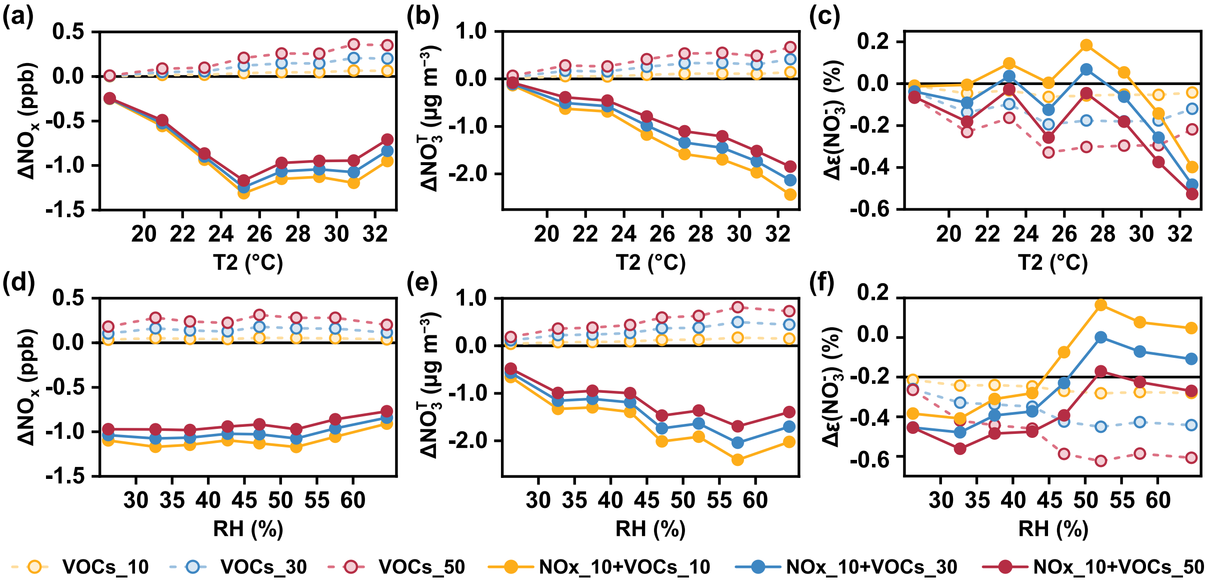

Fig. 8. As in Fig. 7 but for surface-layer (a, d) NO_x (units: ppb), (b, e) NO_3^T (units: μg m^{-3}), and (c, f) NO_3^- particle fraction [$\varepsilon(NO_3^-) = \text{n-}NO_3^- / (\text{n-}HNO_3 + \text{n-}NO_3^-)$; units: %].

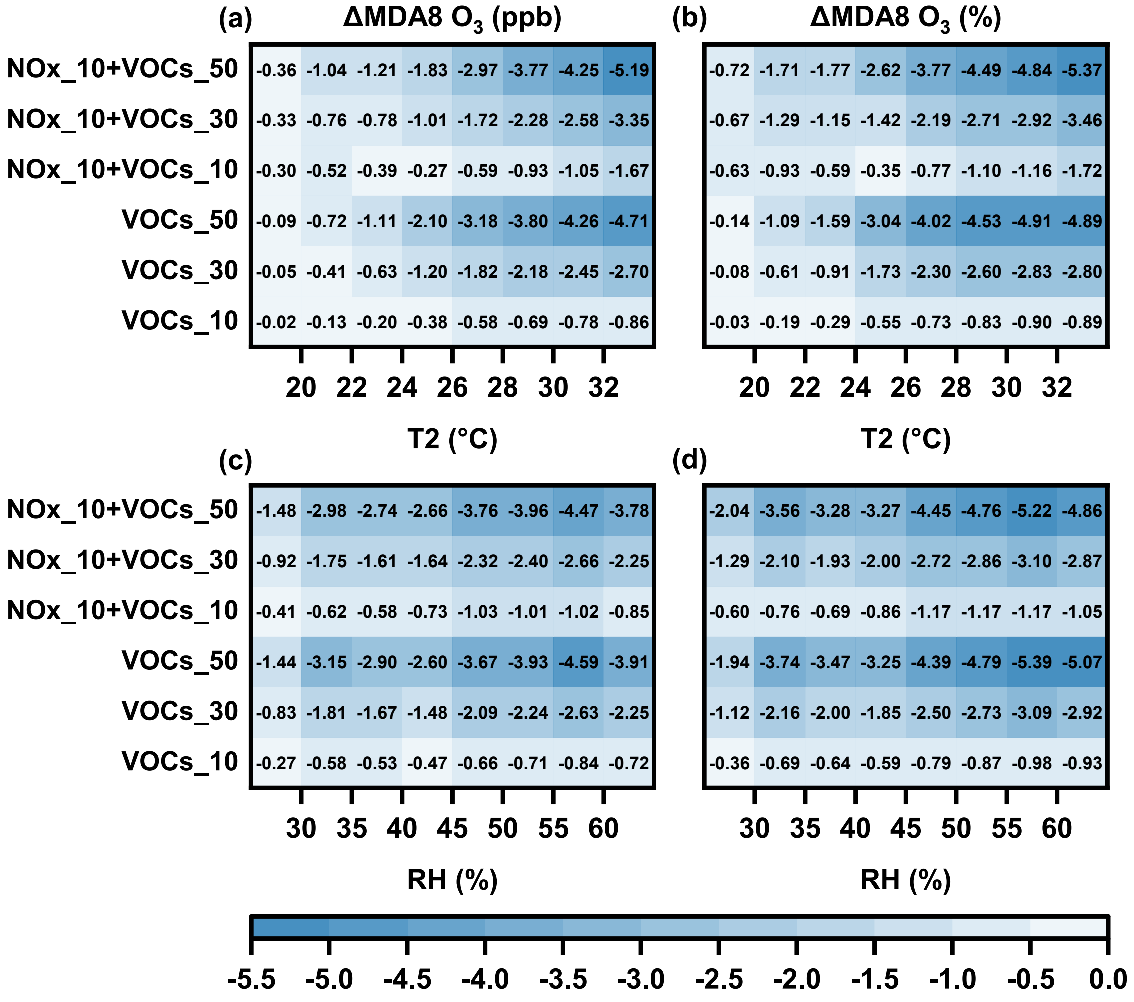

(a) ΔMDA8 O_3 (ppb)

NOx_10+VOCs_50	-0.36	-1.04	-1.21	-1.83	-2.97	-3.77	-4.25	-5.19
NOx_10+VOCs_30	-0.33	-0.76	-0.78	-1.01	-1.72	-2.28	-2.58	-3.35
NOx_10+VOCs_10	-0.30	-0.52	-0.39	-0.27	-0.59	-0.93	-1.05	-1.67
VOCs_50	-0.09	-0.72	-1.11	-2.10	-3.18	-3.80	-4.26	-4.71
VOCs_30	-0.05	-0.41	-0.63	-1.20	-1.82	-2.18	-2.45	-2.70
VOCs_10	-0.02	-0.13	-0.20	-0.38	-0.58	-0.69	-0.78	-0.86

(b) ΔMDA8 O_3 (%)

NOx_10+VOCs_50	-0.72	-1.71	-1.77	-2.62	-3.77	-4.49	-4.84	-5.37
NOx_10+VOCs_30	-0.67	-1.29	-1.15	-1.42	-2.19	-2.71	-2.92	-3.46
NOx_10+VOCs_10	-0.63	-0.93	-0.59	-0.35	-0.77	-1.10	-1.16	-1.72
VOCs_50	-0.14	-1.09	-1.59	-3.04	-4.02	-4.53	-4.91	-4.89
VOCs_30	-0.08	-0.61	-0.91	-1.73	-2.30	-2.60	-2.83	-2.80
VOCs_10	-0.03	-0.19	-0.29	-0.55	-0.73	-0.83	-0.90	-0.89

(c)

NOx_10+VOCs_50	-1.48	-2.98	-2.74	-2.66	-3.76	-3.96	-4.47	-3.78
NOx_10+VOCs_30	-0.92	-1.75	-1.61	-1.64	-2.32	-2.40	-2.66	-2.25
NOx_10+VOCs_10	-0.41	-0.62	-0.58	-0.73	-1.03	-1.01	-1.02	-0.85
VOCs_50	-1.44	-3.15	-2.90	-2.60	-3.67	-3.93	-4.59	-3.91
VOCs_30	-0.83	-1.81	-1.67	-1.48	-2.09	-2.24	-2.63	-2.25
VOCs_10	-0.27	-0.58	-0.53	-0.47	-0.66	-0.71	-0.84	-0.72

(d)

NOx_10+VOCs_50	-2.04	-3.56	-3.28	-3.27	-4.45	-4.76	-5.22	-4.86
NOx_10+VOCs_30	-1.29	-2.10	-1.93	-2.00	-2.72	-2.86	-3.10	-2.87
NOx_10+VOCs_10	-0.60	-0.76	-0.69	-0.86	-1.17	-1.17	-1.17	-1.05
VOCs_50	-1.94	-3.74	-3.47	-3.25	-4.39	-4.79	-5.39	-5.07
VOCs_30	-1.12	-2.16	-2.00	-1.85	-2.50	-2.73	-3.09	-2.92
VOCs_10	-0.36	-0.69	-0.64	-0.59	-0.79	-0.87	-0.98	-0.93

Fig. 9. (a, c) Absolute (units: ppb) and (b, d) percentage changes (units: %) in MDA8 O_3 concentrations in each T2 or RH bin in the 18 grid cells of BTH in JJA 2019 (620 valid samples) in the VOCs_10, VOCs_30, VOCs_50, NO_x_10+VOCs_10, NO_x_10+VOCs_30, and NO_x_10+VOCs_50 simulations (from bottom to top) relative to the CTRL simulation.

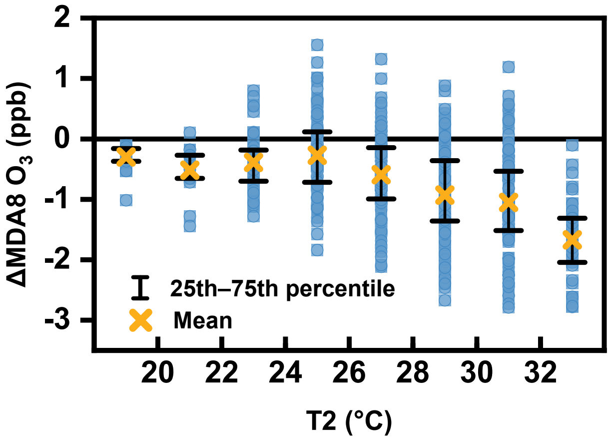

Fig. 10. Boxplots of absolute changes (units: ppb) in MDA8 O_3 concentrations in each T2 bin in the 18 grid cells of BTH in JJA 2019 for all valid samples in the NO_x_10+VOCs_10 simulation relative to the CTRL simulation.

in $PM_{2.5}$ concentrations under different temperature and humidity conditions in JJA 2019 in the 18 grid cells of BTH resulting from emission reductions. By reducing VOC emissions, the highest and second largest values of $\Delta PM_{2.5}$ concentrations occurred when T2 was above 32°C and with the range of 26°C–28°C, respectively. With simultaneous reductions in NO_x and VOC emissions, the absolute and percentage reductions in $PM_{2.5}$ mostly became larger as T2 increased. The highest reductions in mean concentrations were 1.1 (3.5%), 1.0 (3.3%), and 0.9 μg m^{-3} (3.0%) in the bin of > 32°C in the NO_x_10+VOCs_10, NO_x_10+VOCs_30, and NO_x_10+VOCs_50 simulations, respectively.

Reducing 10% of NO_x emissions with 10%, 30%, and 50% of VOC emissions were simulated to result in the highest reductions of 1.6, 1.4, and 1.2 μg m^{-3}, respectively, in mean concentrations of $PM_{2.5}$ in the bin of 55%–60%. The simulated largest percentage decreases in mean $PM_{2.5}$ concentrations occurred when RH was above 60%, with values of 3.7%, 3.2%, and 2.8% in the NO_x_10+VOCs_10, NO_x_10+VOCs_30, and NO_x_10+VOCs_50 simulations, respectively.

It is clearly shown that simultaneous reductions in NO_x and VOC emissions could alleviate $PM_{2.5}$ pollution, but reductions in VOC emissions alone exacerbates $PM_{2.5}$ pollution. Reducing a smaller proportion of VOC emissions will result

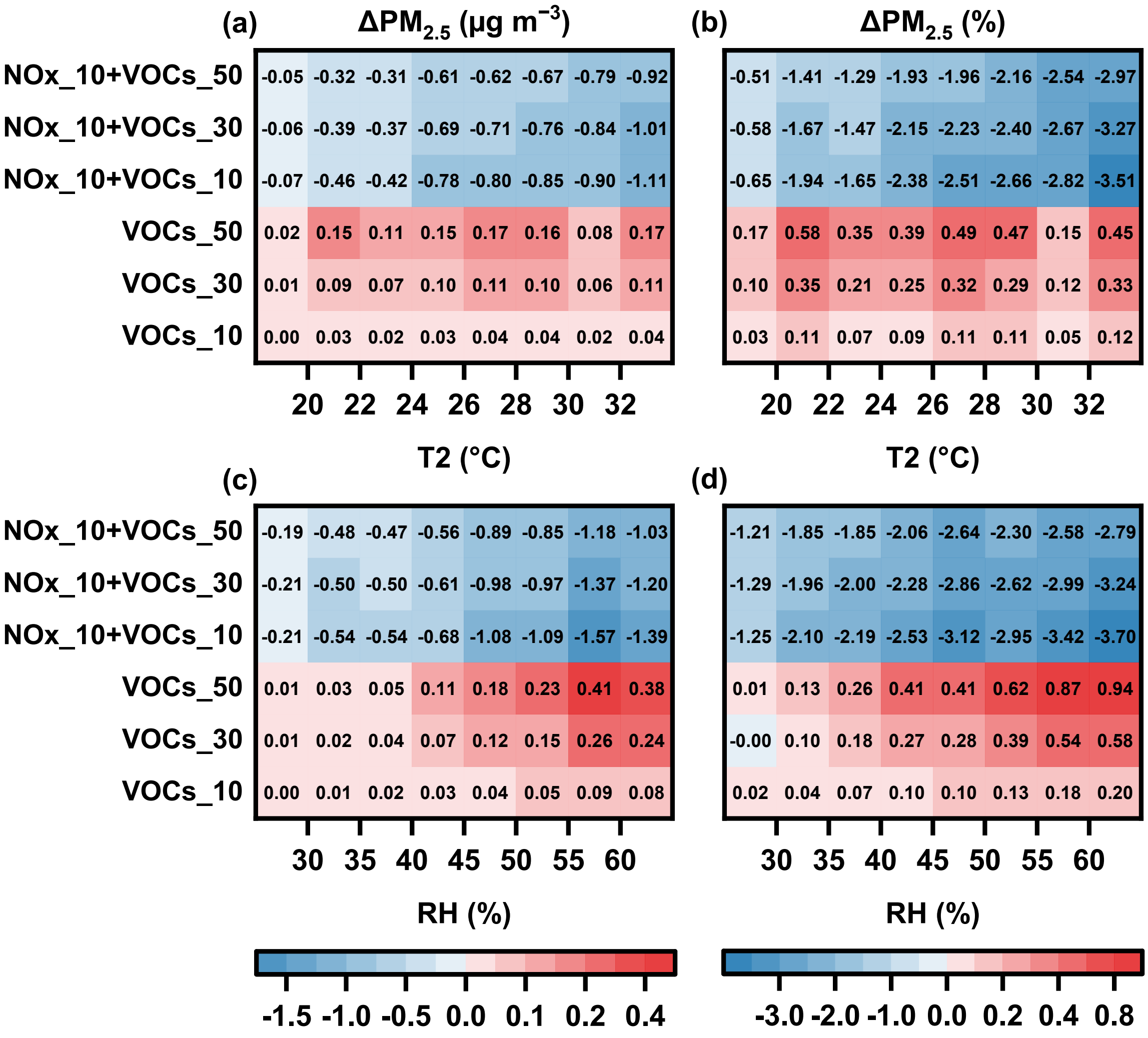

Fig. 11. As in Fig. 9 but for $PM_{2.5}$. The unit of absolute change is μg m^{-3}.

in a smaller increase in $PM_{2.5}$ concentrations in cases of reducing VOC emissions alone, and a larger decrease in cases of simultaneously reducing NO_x and VOC emissions. When RH was above 55%, the control measures on VOC emissions were simulated to lead to the highest decreases in $PM_{2.5}$.

3.4.4. *Impact of precursor emission reductions on $PM_{2.5}$ component concentrations*

The absolute and percentage changes in secondary components of $PM_{2.5}$ in each T2 and RH bin are presented in Figs. 12 and 13, respectively.

3.4.4.1. SOA

All of the six emission reduction measures led to reductions in SOA concentrations. As T2 increased, the reductions in mean SOA concentrations became larger, consistent with the reductions in O_3 and NO_3 concentrations (Figs. 7b and c), with the highest reductions of 4.6×10^{-2} (3.0%), 0.1 (8.8%), 0.2 (14.5%), 3.3×10^{-2} (2.1%), 0.1 (8.1%), and 0.2 μg m^{-3} (14.0%) in the simulations of VOCs_10, VOCs_30, VOCs_50, NO_x_10+VOCs_10, NO_x_10+VOCs_30, and NO_x_10+VOCs_50, respectively. With respect to the results in RH intervals, the maximum absolute (percentage) decreases in mean SOA concentrations of 2.9×10^{-2}–0.2 μg m^{-3} (2.1%–15.8%) occurred at RH of 55%–60% (above 60%), when the average concentrations of O_3 had the highest (second highest) declines (Fig. 7f). Compared to the cases with reductions in both NO_x and VOC emissions, reducing VOC emissions alone resulted in greater reductions in SOA concentration due to the larger decreases in O_3 and NO_3 as well as the smaller increases in OH (Fig. 7).

3.4.4.2. Sulfate

In contrast to SOA, the six emission reduction measures all promoted increases in SO_4^{2-}. Controlling the emissions of NO_x and VOCs led to increases in OH radicals (Figs. 7a and e), which enhanced the gas-phase oxidation of SO_2 and resulted in increases in SO_4^{2-}. Both the absolute and percentage increases of SO_4^{2-} concentrations gradually increased as T2 went up, with the maximum being 3.6×10^{-2}–0.2 μg m^{-3} and 0.6%–2.7%, respectively, except in the NO_x_10+VOCs_10 simulation. In the five cases mentioned above, the positive changes of SOR were highest when T2 was above 32°C (Fig. 7d). In the NO_x_10+VOCs_10 simulation, the highest absolute (percentage) increases occurred when T2 was 26°C–28°C (24°C–26°C), when the increase in OH radicals was second highest (highest) (Fig. 7a). In cases with reductions of VOC emissions alone (both NO_x and VOC emissions), the highest absolute and percentage increases in SO_4^{2-} concentrations occurred at RH of 50%–60% (> 55%), consistent with the changes in SOR (Fig. 7h). In each T2 and RH bin, the absolute (percentage) increases in SO_4^{2-} were positively correlated with the percentage reduction in VOC emissions.

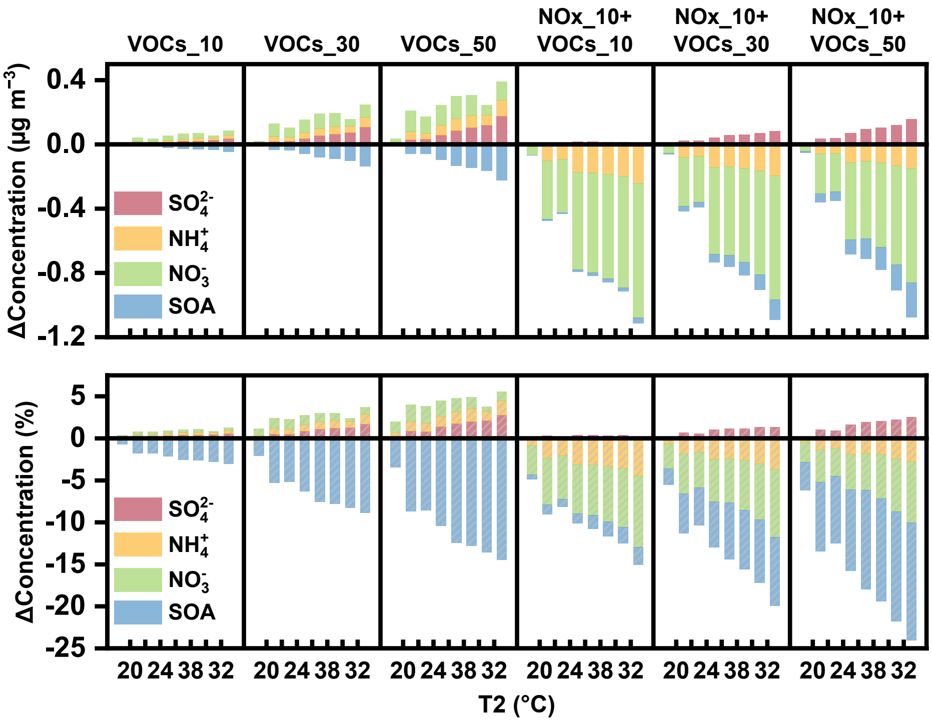

Fig. 12. Absolute (units: μg m^{-3}) and percentage changes (units: %) in concentrations of $PM_{2.5}$ secondary components (SO_4^{2-}, NO_3^-, NH_4^+, and SOA) in each T2 bin in the 18 grid cells of BTH in JJA 2019 (620 valid samples) in the VOCs_10, VOCs_30, VOCs_50, NO_x_10+VOCs_10, NO_x_10+VOCs_30, and NO_x_10+VOCs_50 simulations (from left to right) relative to the CTRL simulation.

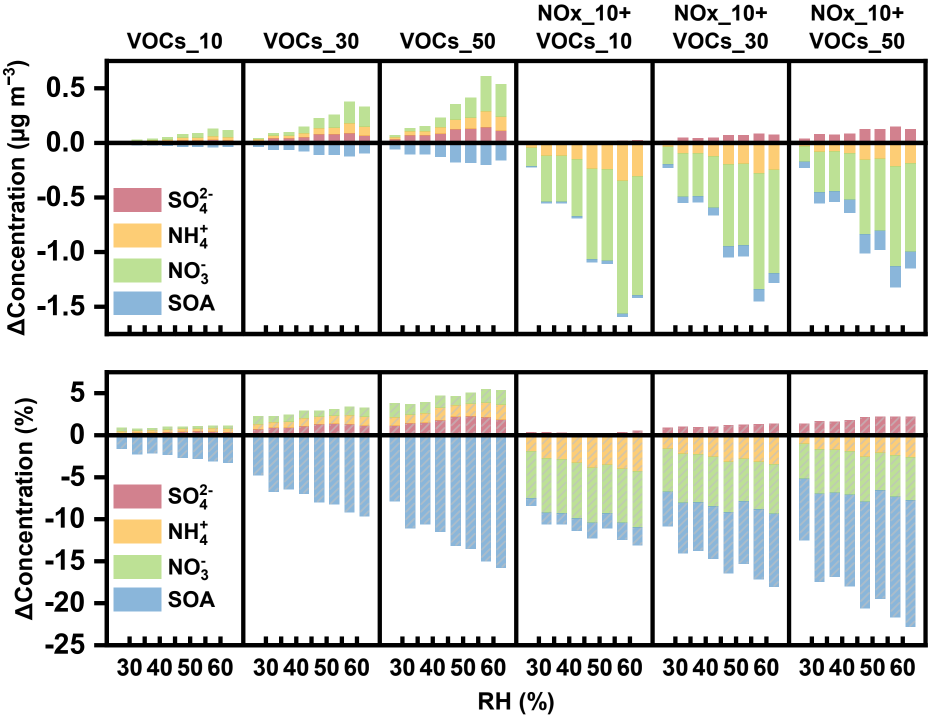

Fig. 13. As in Fig. 12 but for each RH bin.

3.4.4.3. Nitrate

In the simulations with reductions of VOC emissions alone, the higher the proportion of VOCs reduction, the larger the increase in NO_3^- concentration. The increases of OH radicals promoted the formation of HNO_3 during daytime, while the formation of HNO_3 at nighttime through hydrolysis was reduced due to lower N_2O_5 from the decreases in O_3. The daily concentrations of NO_3^T increased as shown in Figs. 8b and e. Sulfate and nitrate compete for NH_3, so the enhanced SO_4^{2-} formation consumed more NH_3, resulting in a decrease in the proportion allocated to the particle phase in NO_3^T [as shown in the NO_3^- particle fraction ($\epsilon(NO_3^-) = \text{n-}NO_3^- / (\text{n-}HNO_3 + \text{n-}NO_3^-)$) in Figs. 8c and f]. However, since NO_3^T was increased, there was still a slight increase in the daily concentration of NO_3^-. Averaged over each T2 bin, the highest absolute (percentage) increases in NO_3^- concentrations occurred when T2 was 26°C–28°C (20°C–24°C), with values of 3.2×10^{-2} (0.4%), 9.1×10^{-2} (1.2%), and 0.1 μg m^{-3} (2.0%) in the VOCs_10, VOCs_30, VOCs_50 simulations relative to the CTRL simulation, respectively. When T2 was 20°C–22°C and 22°C–24°C, the increases in OH radicals were highest and second highest, respectively (Fig. 7a), leading to large formation of HNO_3 and NO_3^-. As for each RH interval, the highest absolute (percentage) increases occurred when RH was 55%–60% (above 60%), with values of 6.8×10^{-2}–0.3 μg m^{-3} (0.4%–1.7%).

With simultaneous reductions in NO_x and VOC emissions, the daytime and nighttime formation of HNO_3 both slowed down due to the reductions in NO_x and O_3 concentrations, inhibiting the generation of NO_3^T and leading to the decreases in daily concentrations of NO_3^-. The smaller proportion of VOCs reduction resulted in the larger decreases in NO_3^- concentrations due to the smaller increases in OH (Figs. 7a and e) and the larger decreases in NO_x (Figs. 8a and d), which inhibited both daytime and nighttime HNO_3 formation more significantly. As T2 went up, the reductions in mean NO_3^- concentration exhibited higher efficiency (larger reductions), consistent with the reductions in O_3 and NO_3 concentrations (Figs. 7b and c). The highest reductions were simulated to be 0.8 (8.5%), 0.8 (8.1%), and 0.7 μg m^{-3} (7.3%) in the simulations of NO_x_10+VOCs_10, NO_x_10+VOCs_30, and NO_x_10+VOCs_50, respectively. Averaged over each RH bin, the highest reductions in NO_3^- concentrations occurred when RH was 55%–60% (the RH bin with the largest decrease in mean O_3 concentration), with values of 1.2, 1.1, and 0.9 μg m^{-3} in the NO_x_10+VOCs_10, NO_x_10+VOCs_30, and NO_x_10+VOCs_50 simulations relative to the CTRL simulation, respectively.

3.4.4.4. Ammonium

The reductions in emissions of VOCs and NO_x affect the concentrations of NH_4^+ through the formation of SO_4^{2-} and NO_3^-. Reducing VOC emissions alone (NO_x and VOC emissions simultaneously) resulted in an increase (a decrease) in NH_4^+ concentrations. As T2 increased, the increases (decreases) in mean NH_4^+ concentrations became larger in both cases. The highest reductions in mean NH_4^+ concentrations were simulated to be 0.1–0.2 μg m^{-3} (2.8%–4.5%) with the simultaneous reductions in NO_x and VOC emissions. For each RH interval, the highest absolute and percentage increases (decreases) in mean NH_4^+ concentrations occurred when RH was 55%–60% and above 60% in both cases, respectively.

Overall, simultaneously reducing NO_x and VOC emissions alleviated $PM_{2.5}$ pollution effectively, especially with a smaller proportion of VOCs reduction. With simultaneous reductions in NO_x and VOC emissions, although there was a positive correlation between the decrease in SOA concentrations and the percentage reduction of VOC emissions, the impact of SOA changes on the level of $PM_{2.5}$ was weak due to its small proportion in $PM_{2.5}$. Smaller percentage reductions in VOCs resulted in smaller increases in SO_4^{2-} concentrations due to the smaller increases in OH radicals, and led to higher decreases in NO_3^- concentrations owing to the larger reduction in both daytime and nighttime formation of HNO_3 caused by the larger decrease in NO_x. At higher temperatures, simultaneous reductions in NO_x and VOC emissions generated more SO_4^{2-} but significantly suppressed the generation of SOA, NO_3^-, and NH_4^+ due to the larger decreases in O_3 and NO_3, leading to larger reductions in $PM_{2.5}$ concentrations. When RH was above 55%, the absolute and percentage decreases in $PM_{2.5}$ concentrations reached their maximum values, caused by the highest reductions in SOA, NO_3^-, and NH_4^+ concentrations due to the highest reduction in O_3 concentrations.

4. Conclusions

We used the observed hourly concentrations of O_3 and $PM_{2.5}$ from MEE, meteorological parameters from MERRA-2, and model results from the nested-grid version of the GEOS-Chem model to examine the relationships between O_3, $PM_{2.5}$, and $PM_{2.5}$ components and T2 or RH over the BTH region and to investigate the effectiveness of precursor emission reductions on O_3 and $PM_{2.5}$ in BTH under different temperature and humidity conditions in the summer of 2019.

Both observed (simulated) MDA8 O_3 and $PM_{2.5}$ concentrations were found to increase as T2 went up, with linear trends of 4.8 (3.2) ppb °C^{-1} and 1.9 (1.5) μg m^{-3} °C^{-1}, respectively. Atmospheric oxidation capacity was stronger at higher temperature, resulting in the increases in $PM_{2.5}$ secondary components. As RH increased, concentrations of $PM_{2.5}$ secondary components increased first and then decreased. SOA peaked at RH of 45%–50% when O_x and NO_3 were at a high level, while SO_4^{2-}, NO_3^-, and NH_4^+ peaked at RH of 55%–60%. There was a bimodal trend in observed or simulated MDA8 O_3 concentrations (peaking at 30%–35% and 45%–50% or 30%–35% and 55%–60%). Both observed and simulated $PM_{2.5}$ concentrations peaked at RH of 55%–60%.

The results of the six sensitivity experiments showed that implementing precursor emission reductions can effectively mitigate summer O_3 pollution in BTH. The larger the percentage reductions of VOC emissions, the larger the reductions in MDA8 O_3. As T2 went up, the absolute values of ΔMDA8 O_3 showed an overall increasing trend, with the maximum values of 0.9–5.2 ppb at a T2 of > 32°C in the six simulations. The percentage reductions in MDA8 O_3 were the largest at a T2 of 30°C–32°C with reductions in VOC emissions alone (0.9%–4.9%), and at a T2 of > 32°C with simultaneous reductions in NO_x and VOCs (1.7%–5.4%). When RH increased, the decreases in MDA8 O_3 concentrations exhibited a bimodal trend. Among the six simulations, the largest decreases in MDA8 O_3 [4.6 ppb (5.4%)] occurred at RH of 55%–60% with a 50% reduction in VOC emissions.

Different from the responses of O_3, reducing VOC emissions alone exacerbated $PM_{2.5}$ pollution. Simultaneous reductions in NO_x and VOC emissions alleviated summer $PM_{2.5}$ pollution in BTH. Reducing a smaller proportion of VOCs resulted in a larger decrease in $PM_{2.5}$ concentration, driven by the larger decrease in NO_3^- concentration due to the larger reduction in both daytime and nighttime formation of HNO_3 from the larger decrease in NO_x. As T2 increased, reductions in $PM_{2.5}$ mostly became larger, with peak values of 1.1 (3.5%), 1.0 (3.3%), and 0.9 μg m^{-3} (3.0%) at a T2 of > 32°C, respectively, in the NO_x_10+VOCs_10, NO_x_10+VOCs_30, and NO_x_10+VOCs_50 simulations. When T2 was above 32°C, the reductions in SOA, NO_3^-, and NH_4^+ concentrations reached their maximum values owing to the large decreases in O_3 and NO_3. As for the RH intervals, the highest absolute reduction in $PM_{2.5}$ concentrations (1.2–1.6 μg m^{-3}) occurred at RH of 55%–60% and the highest percentage reduction (2.8%–3.7%) occurred in the bin of > 60% with simultaneous reductions in NO_x and VOCs. At RH of > 55%, the large reductions in O_3 contributed to the large reductions in SOA, NO_3^-, and NH_4^+ concentrations.

In summary, reducing a larger proportion of VOC emissions can lead to a larger reduction in MDA8 O_3 in BTH during summer. The decreases in MDA8 O_3 caused by precursor emission reductions are more sensitive to T2 than to RH. Higher reductions of VOC emissions at higher T2 is more effective for alleviating summer O_3 pollution in BTH. When $PM_{2.5}$ pollution is a concern in summer, NO_x reduction combined with a small proportion of reduction in VOCs is the best measure. The reduction in $PM_{2.5}$ from reducing precursor emissions is more sensitive to RH than to T2, with the best efficiency at high RH. For the control of co-pollution of O_3 and $PM_{2.5}$ in summer in BTH, precursor emission reductions have the best effect in hot and humid conditions.

Acknowledgements. This work was supported by the National Natural Science Foundation of China (Grant No. 91744311).

REFERENCES

Alexander, B., R. J. Park, D. J. Jacob, Q. B. Li, R. M. Yantosca, J. Savarino, C. C. W. Lee, and M. H. Thiemens, 2005: Sulfate formation in sea-salt aerosols: Constraints from oxygen isotopes. *J. Geophys. Res.: Atmos.*, **110**, D10307, https://doi.org/10.1029/2004JD005659.

Bey, I., and Coauthors, 2001: Global modeling of tropospheric chemistry with assimilated meteorology: Model description and evaluation. *J. Geophys. Res.: Atmos.*, **106**, 23 073–23 095, http://doi.org/10.1029/2001jd000807.

Chen, L., J. Zhu, H. Liao, Y. Yang, and X. Yue, 2020: Meteorological influences on $PM_{2.5}$ and O_3 trends and associated health burden since China's clean air actions. *Science of the Total Environment*, **744**, 140837, https://doi.org/10.1016/j.scitotenv.2020.140837.

Cooke, W. F., C. Liousse, H. Cachier, and J. Feichter, 1999: Construction of a 1° × 1° fossil fuel emission data set for carbonaceous aerosol and implementation and radiative impact in the ECHAM4 model. *J. Geophys. Res.: Atmos.*, **104**, 22 137–22 162, http://doi.org/10.1029/1999JD900187.

Dai, H. B., H. Liao, Y. Wang, and J. Qian, 2024: Co-occurrence of ozone and $PM_{2.5}$ pollution in urban/non-urban areas in eastern China from 2013 to 2020: Roles of meteorology and anthropogenic emissions. *Science of the Total Environment*, **924**, 171687, https://doi.org/10.1016/j.scitotenv.2024.171687.

Dai, H. B., and Coauthors, 2023: Composited analyses of the chemical and physical characteristics of co-polluted days by ozone and $PM_{2.5}$ over 2013–2020 in the Beijing–Tianjin–Hebei region. *Atmospheric Chemistry and Physics*, **23**, 23–39, https://doi.org/10.5194/acp-23-23-2023.

Dang, R. J., and H. Liao, 2019: Severe winter haze days in the Beijing–Tianjin–Hebei region from 1985 to 2017 and the roles of anthropogenic emissions and meteorology. *Atmospheric Chemistry and Physics*, **19**, 10 801–10 816, https://doi.org/10.5194/acp-19-10801-2019.

Dang, R. J., H. Liao, and Y. Fu, 2021: Quantifying the anthropogenic and meteorological influences on summertime surface ozone in China over 2012–2017. *Science of the Total Environment*, **754**, 142394, https://doi.org/10.1016/j.scitotenv.2020.142394.

Dawson, J. P., P. J. Adams, and S. N. Pandis, 2007: Sensitivity of $PM_{2.5}$ to climate in the Eastern US: A modeling case study. *Atmospheric Chemistry and Physics*, **7**, 4295–4309, https://doi.org/10.5194/acp-7-4295-2007.

Ding, D., J. Xing, S. X. Wang, Z. X. Dong, F. F. Zhang, S. C. Liu, and J. M. Hao, 2022: Optimization of a NO_x and VOC cooperative control strategy based on clean air benefits. *Environ. Sci. Technol.*, **56**, 739–749, https://doi.org/10.1021/acs.est.1c04201.

Dong, X. Y., J. Li, J. S. Fu, Y. Gao, K. Huang, and G. S. Zhuang, 2014: Inorganic aerosols responses to emission changes in Yangtze River Delta, China. *Science of the Total Environment*, **481**, 522–532, https://doi.org/10.1016/j.scitotenv.2014.02.076.

Fairlie, T. D., D. J. Jacob, and R. J. Park, 2007: The impact of transpacific transport of mineral dust in the United States. *Atmos. Environ.*, **41**, 1251–1266, http:// https://doi.org/10.1016/j.atmosenv.2006.09.048.

Feng, T., and Coauthors, 2019: Secondary organic aerosol enhanced by increasing atmospheric oxidizing capacity in Beijing–Tianjin–Hebei (BTH), China. *Atmospheric Chemistry and Physics*, **19**, 7429–7443, https://doi.org/10.5194/acp-19-7429-2019.

Fu, Y., and H. Liao, 2014: Impacts of land use and land cover changes on biogenic emissions of volatile organic compounds in China from the late 1980s to the mid-2000s: Implications for tropospheric ozone and secondary organic aerosol. *Tellus B: Chemical and Physical Meteorology*, **66**, 24987, https://doi.org/10.3402/tellusb.v66.24987.

Gelaro, R., and Coauthors, 2017: The modern-era retrospective analysis for research and applications, version 2 (MERRA-2). *J. Climate*, **30**, 5419–5454, https://doi.org/10.1175/JCLI-D-16-0758.1.

Gong, C., Y. Wang, H. Liao, P. Y. Wang, J. B. Jin, and Z. W. Han, 2022: Future co-occurrences of hot days and ozone-polluted days over China under scenarios of shared socioeconomic pathways predicted through a machine-learning approach. *Earth's Future*, **10**, e2022EF002671, https://doi.org/10.1029/2022EF002671.

Guenther, A. B., X. Jiang, C. L. Heald, T. Sakulyanontvittaya, T. Duhl, L. K. Emmons, and X. Wang, 2012: The Model of Emissions of Gases and Aerosols from Nature version 2.1 (MEGAN2.1): An extended and updated framework for modeling biogenic emissions. *Geoscientific Model Development*, **5**, 1471–1492, https://doi.org/10.5194/gmd-5-1471-2012.

Jacob, D. J., and D. A. Winner, 2009: Effect of climate change on air quality. *Atmos. Environ.*, **43**, 51–63, https://doi.org/10.1016/j.atmosenv.2008.09.051.

Jo, D. S., R. J. Park, M. J. Kim, and D. V. Spracklen, 2013: Effects of chemical aging on global secondary organic aerosol using the volatility basis set approach. *Atmos. Environ.*, **81**, 230–244, https://doi.org/10.1016/j.atmosenv.2013.08.055.

Johnson, C. E., W. J. Collins, D. S. Stevenson, and R. G. Derwent, 1999: Relative roles of climate and emissions changes on future tropospheric oxidant concentrations. *J. Geophys. Res.: Atmos.*, **104**, 18 631–18 645, https://doi.org/10.1029/1999jd900204.

Kang, M. J., J. Zhang, H. L. Zhang, and Q. Ying, 2021: On the Relevancy of observed ozone increase during COVID-19 lockdown to summertime ozone and $PM_{2.5}$ control policies in China. *Environmental Science & Technology Letters*, **8**, 289–294, https://doi.org/10.1021/acs.estlett.1c00036.

Kleeman, M. J., 2008: A preliminary assessment of the sensitivity of air quality in California to global change. *Climatic Change*, **87**, 273–292, https://doi.org/10.1007/s10584-007-9351-3.

Lee, B. H., J. R. Pierce, G. J. Engelhart, and S. N. Pandis, 2011: Volatility of secondary organic aerosol from the ozonolysis of monoterpenes. *Atmos. Environ.*, **45**, 2443–2452, https://doi.org/10.1016/j.atmosenv.2011.02.004.

Leung, D. M., and Coauthors, 2020: Wintertime particulate matter decrease buffered by unfavorable chemical processes despite emissions reductions in China. *Geophys. Res. Lett.*, **47**, e2020GL087721, https://doi.org/10.1029/2020GL087721.

Li, K., D. J. Jacob, H. Liao, L. Shen, Q. Zhang, and K. H. Bates, 2019a: Anthropogenic drivers of 2013–2017 trends in summer surface ozone in China. *Proceedings of the National Academy of Sciences of the United States of America*, **116**, 422–427, https://doi.org/10.1073/pnas.1812168116.

Li, K., D. J. Jacob, L. Shen, X. Lu, I. De Smedt, and H. Liao, 2020: Increases in surface ozone pollution in China from 2013 to 2019: Anthropogenic and meteorological influences. *Atmospheric Chemistry and Physics*, **20**, 11 423–11 433, https://doi.org/10.5194/acp-20-11423-2020.

Li, K., and Coauthors, 2019b: A two-pollutant strategy for improving ozone and particulate air quality in China. *Nature Geoscience*, **12**, 906–910, https://doi.org/10.1038/s41561-019-0464-x.

Li, K., and Coauthors, 2021: Ozone pollution in the North China Plain spreading into the late-winter haze season. *Proceedings of the National Academy of Sciences of the United States of America*, **118**, e2015797118, https://doi.org/10.1073/pnas.2015797118.

Liao, H., W. T. Chen, and J. H. Seinfeld, 2006: Role of climate change in global predictions of future tropospheric ozone and aerosols. *J. Geophys. Res.: Atmos.*, **111**, D12304, https://doi.org/10.1029/2005JD006852.

Liu, H. Y., D. J. Jacob, I. Bey, and R. M. Yantosca, 2001: Constraints from ^{210}Pb and ^{7}Be on wet deposition and transport in a global three-dimensional chemical tracer model driven by assimilated meteorological fields. *J. Geophys. Res.: Atmos.*, **106**, 12 109–12 128, http://doi.org/10.1029/2000jd900839.

Liu, S., J. Xing, H. L. Zhang, D. Ding, F. F. Zhang, B. Zhao, S. K. Sahu, and S. X. Wang, 2019: Climate-driven trends of biogenic volatile organic compound emissions and their impacts on summertime ozone and secondary organic aerosol in China in the 2050s. *Atmos. Environ.*, **218**, 117020, https://doi.org/10.1016/j.atmosenv.2019.117020.

Luo, Y. H., and Coauthors, 2022: Seasonal changes in the recent decline of combined high $PM_{2.5}$ and O_3 pollution and associated chemical and meteorological drivers in the Beijing–Tianjin–Hebei region, China. *Science of the Total Environment*, **838**, 156312, https://doi.org/10.1016/j.scitotenv.2022.156312.

Park, R. J., D. J. Jacob, M. Chin, and R. V. Martin, 2003: Sources of carbonaceous aerosols over the United States and implications for natural visibility. *J. Geophys. Res.: Atmos.*, **108**, D124355, http:// https://doi.org/10.1029/2002JD003190.

Park, R. J., D. J. Jacob, B. D. Field, R. M. Yantosca, and M. Chin, 2004: Natural and transboundary pollution influences on sulfate-nitrate-ammonium aerosols in the United States: Implications for policy. *J. Geophys. Res.: Atmos.*, **109**, D15204, https://doi.org/10.1029/2003JD004473.

Pye, H. O. T., H. Liao, S. Wu, L. J. Mickley, D. J. Jacob, D. K. Henze, and J. H. Seinfeld, 2009: Effect of changes in climate and emissions on future sulfate-nitrate-ammonium aerosol levels in the United States. *J. Geophys. Res.: Atmos.*, **114**, D01205, https://doi.org/10.1029/2008JD010701.

Shah, V., and Coauthors, 2018: Chemical feedbacks weaken the wintertime response of particulate sulfate and nitrate to emissions reductions over the eastern United States. *Proceedings of the National Academy of Sciences of the United States of America*, **115**, 8110–8115, https://doi.org/10.1073/pnas.1803295115.

Tang, M. X., and Coauthors, 2022: Decisive role of ozone formation control in winter $PM_{2.5}$ mitigation in Shenzhen, China. *Environmental Pollution*, **301**, 119027, https://doi.org/10.1016/j.envpol.2022.119027.

Wang, F., and Coauthors, 2022: Machine learning and theoretical analysis release the non-linear relationship among ozone, secondary organic aerosol and volatile organic compounds. *Journal of Environmental Sciences*, **114**, 75–84, https://doi.org/10.1016/j.jes.2021.07.026.

Wang, Y., and H. Liao, 2020: Effect of emission control measures on ozone concentrations in Hangzhou during G20 meeting in 2016. *Chemosphere*, **261**, 127729, https://doi.org/10.1016/j.chemosphere.2020.127729.

Wang, Y., Q. Q. Zhang, K. He, Q. Zhang, and L. Chai, 2013: Sulfate-nitrate-ammonium aerosols over China: Response to 2000–2015 emission changes of sulfur dioxide, nitrogen oxides, and ammonia. *Atmospheric Chemistry and Physics*, **13**, 2635–2652, https://doi.org/10.5194/acp-13-2635-2013.

Wang, Y. H., D. J. Jacob, and J. A. Logan, 1998: Global simulation of tropospheric O_3-NO_x-hydrocarbon chemistry: 1. Model formulation. *J. Geophys. Res.: Atmos.*, **103**, 10 713–10 725, https://doi.org/10.1029/98jd00158.

Wesely, M. L., 1989: Parameterization of surface resistances to gaseous dry deposition in regional-scale numerical models. *Atmos. Environ.*, **23**, 1293–1304, https://doi.org/10.1016/0004-6981(89)90153-4.

Wu, K., and Coauthors, 2020: Estimation of biogenic VOC emissions and their corresponding impact on ozone and secondary organic aerosol formation in China. *Atmospheric Research*, **231**, 104656, https://doi.org/10.1016/j.atmosres.2019.104656.

Xiang, S. L., and Coauthors, 2020: Control of both $PM_{2.5}$ and O_3 in Beijing-Tianjin-Hebei and the surrounding areas. *Atmos. Environ.*, **224**, 117259, https://doi.org/10.1016/j.atmosenv.2020.117259.

Zhang, H. X., C. R. Chen, W. J. Yan, N. N. Wu, Y. Bo, Q. Zhang, and K. B. He, 2021: Characteristics and sources of non-methane VOCs and their roles in SOA formation during autumn in a central Chinese city. *Science of the Total Environment*, **782**, 146802, https://doi.org/10.1016/j.scitotenv.2021.146802.

Zhang, Y., H. Liao, X. Ding, D. Jo, and K. Li, 2018: Implications of RCP emissions on future concentration and direct radiative forcing of secondary organic aerosol over China. *Science of the Total Environment*, **640–641**, 1187–1204, https://doi.org/10.1016/j.scitotenv.2018.05.274.

Zhang, Z. T., and K. C. Wang, 2020: Stilling and recovery of the surface wind speed based on observation, reanalysis, and geostrophic wind theory over China from 1960 to 2017. *J. Climate*, **33**, 3989–4008, https://doi.org/10.1175/jcli-d-19-0281.1.

Zhao, H., K. Y. Chen, Z. Liu, Y. X. Zhang, T. Shao, and H. L. Zhang, 2021: Coordinated control of $PM_{2.5}$ and O_3 is urgently needed in China after implementation of the "Air pollution prevention and control action plan". *Chemosphere*, **270**, 129441, https://doi.org/10.1016/j.chemosphere.2020.129441.

Zheng, B., and Coauthors, 2015: Heterogeneous chemistry: A mechanism missing in current models to explain secondary inorganic aerosol formation during the January 2013 haze episode in North China. *Atmospheric Chemistry and Physics*, **15**, 2031–2049, https://doi.org/10.5194/acp-15-2031-2015.

Zheng, B., and Coauthors, 2018: Trends in China's anthropogenic emissions since 2010 as the consequence of clean air actions. *Atmospheric Chemistry and Physics*, **18**, 14 095–14 111, https://doi.org/10.5194/acp-18-14095-2018.

Zhu, J., L. Chen, H. Liao, and R. J. Dang, 2019: Correlations between $PM_{2.5}$ and ozone over China and associated underlying reasons. *Atmosphere*, **10**, 352, https://doi.org/10.3390/atmos10070352.

Zong, L., and Coauthors, 2021: Large-scale synoptic drivers of co-occurring summertime ozone and $PM_{2.5}$ pollution in eastern China. *Atmospheric Chemistry and Physics*, **21**, 9105–9124, https://doi.org/10.5194/acp-21-9105-2021.